LAWRENCE
LIVERMORE
NATIONAL
LABORATORY

UCRL-TR-218130

Calibration of Parameters in Beta-Delta HMX Phase Transformation Kinetics Using Computer Simulations

A. P. Wemhoff, A. K. Burnham

January 13, 2006

This work was performed under the auspices of the U.S. Department of Energy by University of California, Lawrence Livermore National Laboratory under Contract W-7405-Eng-48.

Abstract

The kinetics of the beta-delta solid-solid phase transformation of HMX (nitramine octahydro-1,3,5,7-tetranitro-1,3,5,7-tetrazocine) were modeled in ALE2D using four similar equilibrium-inhibited nucleation-growth models: a reversible set of Arrhenius kinetics following a LANL model, and three sets of kinetics derived based on an autocatalytic model using the bidirectional reaction formalism. The parameters for the bidirectional kinetics models were calibrated using simulations of two experimental setup scenarios where experimental data is available: 165°C XRD and SITI. In this calibration, the transition enthalpy and activation energy values were kept constant, while the frequency factors were iterated to achieve results similar to those provided by the experiments. This process yielded six unique sets of kinetic parameters that describe the phase transformation: a pair of sets for each of the three bidirectional kinetics models. The models calibrated using 165°C XRD data showed good agreement with LX-04 STEX experimental results, while the SITI-based models were in good agreement with the LANL model and PBX-9501 STEX experimental data. These bidirectional models were also shown to require less computational effort than the LANL model.

Table of Contents

Introduction 5

Simulation Setup 6

Thermal Properties of HMX 8

Chemical Kinetics Models 9

Calibration of Bidirectional Kinetics Models 15

Application of Kinetics Models to Various Experimental Setup Scenarios 17

165°C XRD scenario 17

175°C XRD scenario 21

SITI scenario 26

STEX scenario 36

Computational Effort Comparison 45

Conclusions 46

Acknowledgements 47

References 47

Introduction

The chemical kinetics of the ignition of the high explosive (HE) HMX has been of interest to both LANL and LLNL. From the study of the reactions of this material, a solid-solid phase transition is known to occur prior to deflagration. This transition allows the stable phase of HMX (beta phase) to be converted into an unstable phase (delta phase) that may undergo deflagration. The delta phase is more sensitive to shock initiation (Urtiew, 2004). Although the kinetics of the transition has been studied both analytically and experimentally (e.g., Schmitt et al., 2003; Burnham and Weese, 2004; Saw, 2002; Henson et al., 2002), various kinetic models are constantly being introduced as means to more accurately describe the transition.

This study derives preliminary kinetic parameters for three types of bidirectional reaction models that describe the beta-delta phase transition. These derivations were performed using simulations of LLNL's multi-mechanics code, ALE2D, with the objective to see which models would work qualitatively rather than finalize model calibration. The calibrations of kinetics parameters were performed for four experimental setup scenarios, although only two of these four, 165°C X-ray diffraction (XRD) experiments at the Stanford Linear Accelerator Center (SLAC) (Zaug et al., 2003) and the Sandia Instrumented Thermal Ignition (SITI) experiment (Kaneshige et al., 2002) were used to calibrate the phase transition kinetics, while the third (175°C XRD at SLAC) and fourth (Scaled Thermal Explosion Experiment (STEX), Maienschein et al., 2002) were added as a means for comparison of the derived kinetics to each other and a known LANL reversible kinetics model. These four experimental setup scenarios are as follows:

- 165°C XRD: isothermal external 165°C boundary of a long 0.02"-diameter HMX cylinder from a uniform initial temperature of 20°C.
- 175°C XRD: isothermal external 175°C boundary of a long 0.02"-diameter HMX cylinder from a uniform initial temperature of 20°C.
- SITI: external linear ramping of the external boundary of a 1" long × 1" diameter HMX cylinder from 20°C to 192°C at a rate of 7°C/min, and then holding the surface temperature at 192°C. The uniform initial temperature of the cylinder is 20°C.
- STEX: external linear ramping of the external boundary of a 2" diameter HMX cylinder at a fixed rate of 1°C/hr. The uniform initial temperature of the cylinder is 20°C.

The XRD experiments used LLNL B-725 HMX powder (Mason & Hanger Lot 920-27, Grade2, Class A, trimodal particle-size distribution with peaks at ~0.3, 8, and 90 μm). The SITI experiment used PBX-9501 (unspecified lot). The STEX experiments used either HMX formulations from LLNL (LX-10 or LX-04) or from LANL (PBX-9501).

Simulation Setup

The cylindrical geometry of the HMX samples in the various scenarios allowed for the use of the two-dimensional capability of ALE3D (commonly referred to as ALE2D). In these simulations, a two-dimensional mesh is used with a specified axisymmetric geometry along the *x*-axis. The mesh used for each of the three experimental setup scenarios are shown below in Figures 1 through 3. The two-dimensionality of the geometry allows for faster code execution and avoids the inherent stress mechanics problems of wedge-shaped three-dimensional hexahedral elements. Note that the large aspect ratios of the XRD and STEX geometries allow for the omission of end effects, and thus the height of the "strip" was chosen such that the two-dimensional elements would have aspect ratios of unity.

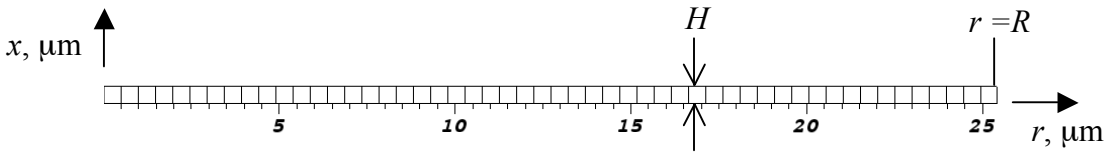

FIGURE 1. Two-dimensional mesh used in XRD experimental setup scenarios.

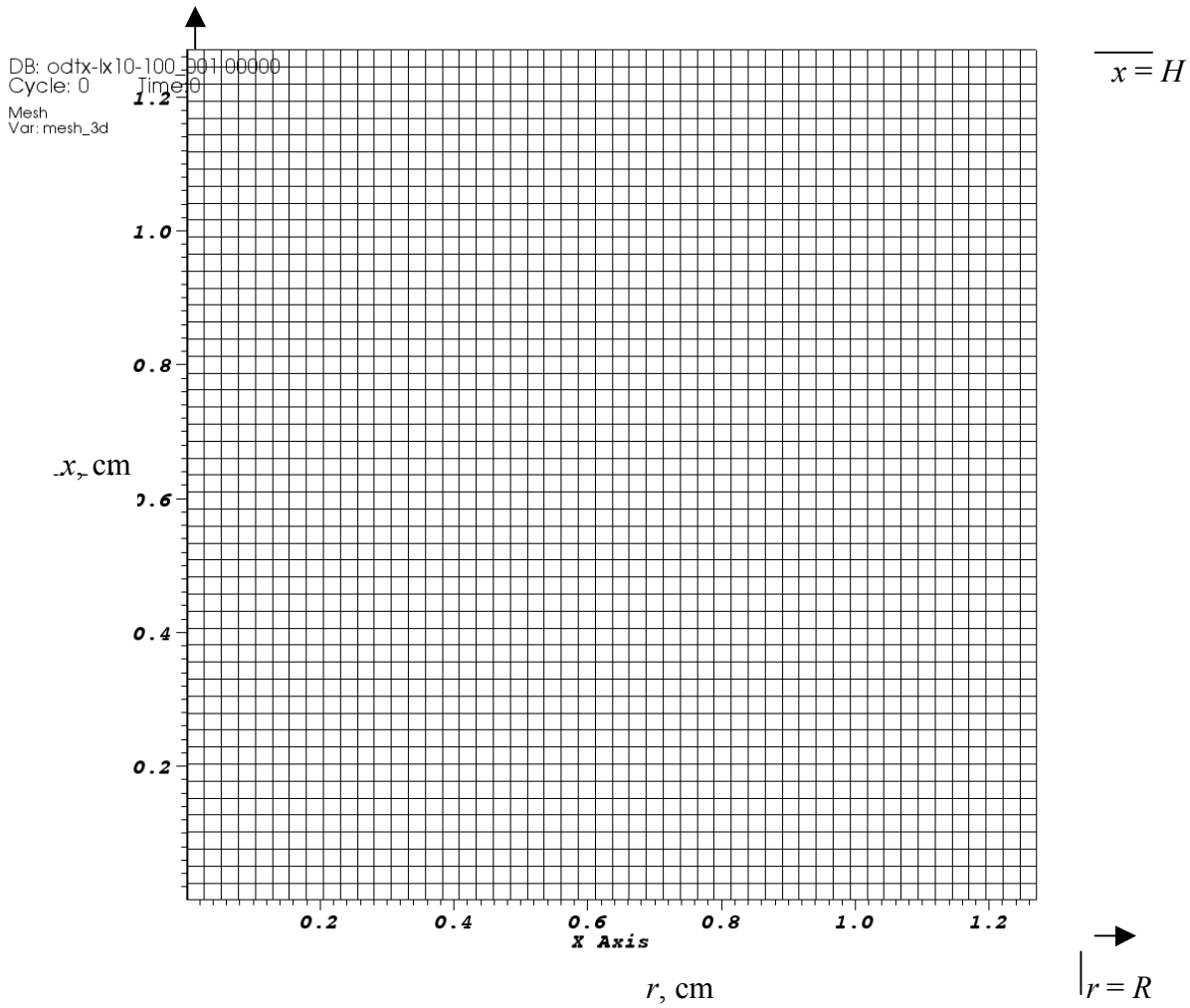

FIGURE 2. Two-dimensional mesh used in SITI experimental setup scenario.

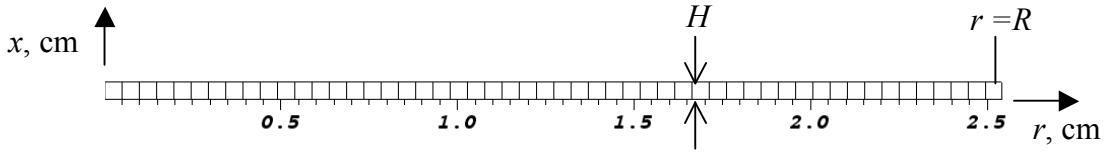

FIGURE 3. Two-dimensional mesh used in STEX experimental setup scenario.

In all of the three experimental setup scenarios, symmetry boundary conditions were used along the *x*-axis and the *r*-axis. In addition, in the mesh geometry for the XRD and SITI experimental setup scenarios, a symmetry boundary condition was used at the $x = H$ boundary. The outside radial surface ($r = R$) of the XRD and STEX geometries experienced an applied ambient pressure. In the SITI geometry, the axial ends of the

mesh geometry ($x = H$) for the SITI experimental setup scenario were kept at atmospheric pressure, but the outer radial surface ($r = R$) was constrained.

Thermal Properties of HMX

It was assumed that the mechanical and thermal properties of the two solid phases, β-HMX and δ-HMX, are equivalent. The thermal properties of solid HMX (heat capacity, thermal conductivity, heat of reaction) were adapted from the model of Tarver and Tran (2004) and are tabulated in Table 1 for use in ALE3D. The HMX material model in ALE2D experienced a variation of density with pressure and temperature according to a 7-term polynomial equation of state for the solid HMX components,

$$P = A_0 + A_1\mu + A_2\mu^2 + A_3\mu^3 + \left(B_0 + B_1\mu + B_2\mu^2\right)E \tag{1}$$

where

$$\mu = \frac{\rho}{\rho_0} - 1$$
$$E = C_v^* T + E_{cold} \tag{2}$$

In the above equations, the coefficients A_i and B_i were previously provided by Jack Yoh for HMX (shown in Table 2), ρ_0 and C_v^* are averaged density and specific heat values, and E_{cold} is the cold energy of the material. The reference state of the materials was chosen such that the energy was zero at a temperature of 110°C and a density of 1.865 g/cm^3. Table 1 shows the density variation in the system assuming zero pressure change.

The enthalpy of formation value of δ-HMX was specified as 7.9 cal/g (33 J/g).

TABLE 1. Thermal Properties of Solid HMX Used in ALE3D.

Temperature, ^{o}C	Thermal conductivity, W/cm/K	Density, g/cm^3	Specific heat, J/g/K
25	0.0053	1.892	1.004
75	0.0051	1.879	1.172
125	0.0049	1.866	1.339
160	0.0046	1.856	1.422
180	0.0044	1.850	1.464
225	0.0041	1.836	1.548
275	0.0039	1.820	1.632

TABLE 2. Coefficients Used in HMX Equation of State.

Parameter	Value
A_0	0.0 MBar
A_1	0.135 MBar
A_2	0.819 MBar
A_3	0. MBar
B_0	1.009 cc^{-1}
B_1	1.009 cc^{-1}
B_2	0.0 cc^{-1}

Chemical Kinetics Models

The simulated sample was initially comprised of 100% β-HMX at 20°C. At time $t = 0$, the external boundary was heated according to each experimental setup scenario. As the temperature of the sample increased, the beta-delta phase transition occurred according to the applied kinetics model. The reaction rates were based on the element-centered temperature and were thus unique to each element in the mesh.

The kinetics models described in this study contained two types of reactions: Arrhenius and bidirectional. An Arrhenius-type reaction is described as

$$k(N,T) = A^0 N^a \exp\left(-\frac{E^*}{RT}\right) \tag{3}$$

where the reaction rate k is dependent upon the mass concentration values N of any subset of possible materials to a unique integer power a. The reaction rate is heavily dependent upon the energy of formation E^* and the temperature T. The ideal gas constant, R, is 1.987 cal/(mol-K).

A modification to the Arrhenius reaction type is the bidirectional type, which is equivalent to multiplying the Arrhenius reaction by a temperature-dependent factor to obtain

$$k(N,T) = A^0 N^a \exp\left(-\frac{E^*}{RT}\right)\sinh\left(\Lambda_e^* - \frac{E_e^*}{RT}\right) \tag{4}$$

Note that the sinh function in equation (4) is an approximation to the model proposed by Burnham (2004),

$$k(N,T) = A^0 N^a \exp\left(-\frac{E^*}{RT}\right)\left(1 - {}^{1}\!/\!_{K_{eq}}\right) \tag{5}$$

where K_{eq} is the equilibrium constant. A similar temperature dependence of equations (4) and (5) may be found by setting both to zero at an equilibrium temperature T_{eq}:

$$\sinh\left(\Lambda_e^* - \frac{E_e^*}{RT_{eq}}\right) \approx 1 - \frac{1}{K_o \exp\left(-\frac{E_e^*}{RT_{eq}}\right)} \tag{6}$$

The two functional relations may be compared using

$$\begin{aligned} \Lambda_e^* &= \frac{E_e^*}{RT_{eq}} = \ln K_o \\ E_e^* &= \Lambda_e^* RT_{eq} \end{aligned} \tag{7}$$

for known values of T_{eq} and K_o. In this study, the values of T_{eq} and K_o used were 160°C and 15.3, respectively.

As its name implies, the bi-directional nature of these reactions provides a major difference to the Arrhenius-type reactions. Therefore, the kinetics models containing these reactions do not need reaction pairs to account for reverse phase transitions, which reduces the number of reactions needed in the kinetic model. Figure 4 shows that for a simple bidirectional beta-to-delta reaction of zero order,

$$\beta \xleftrightarrow{k_{bd}} \delta \tag{8}$$

which results in changes in mass concentration values as

$$\frac{dN_\beta}{dt} = -k_{bd}(T)$$
$$\frac{dN_\delta}{dt} = +k_{bd}(T) \tag{9}$$

where k_{bd} is defined as positive for the transition proceeding from left to right in equation (8), and

$$k_{bd}(T) = A_{bd}^0 \exp\left(-\frac{E^*}{RT}\right)\sinh\left(\Lambda_e^* - \frac{E_e^*}{RT}\right) \tag{10}$$

If an Arrhenius kinetic model were used, then the reaction follows

$$\beta \xrightarrow{k_{ar}} \delta$$

where

$$k_{ar}(T) = A_{ar}^0 \exp\left(-\frac{E^*}{RT}\right) \tag{11}$$

The values of the parameters used in equations (10) and (11) are

$$A_{bd}^0 = A_{ar}^0 = 2.0 \times 10^{36}\,\mathrm{s}^{-1}$$
$$E^* = 57820\,\mathrm{cal/mol}$$
$$E_e^* = 2350\,\mathrm{cal/mol} \tag{12}$$
$$\Lambda_e^* = 2.6247$$

The activation energy E^* and enthalpy E_e^* come from Burnham et al. (2004). In this example, the values of T_{eq} and K_o used were 177.45°C and 13.8, respectively, which where estimated from the work of Landers and Brill (1980). In these simulations, the external temperature is ramped at 10°C/hr from 20°C to 210°C and back to 20°C for a 2" diameter cylinder. Figure 4 shows that the beta-delta phase transition occurs on a temperature ramping process for both the Arrhenius and bidirectional reactions, but then the reverse transition occurs in a cool-down process for only the bidirectional reaction.

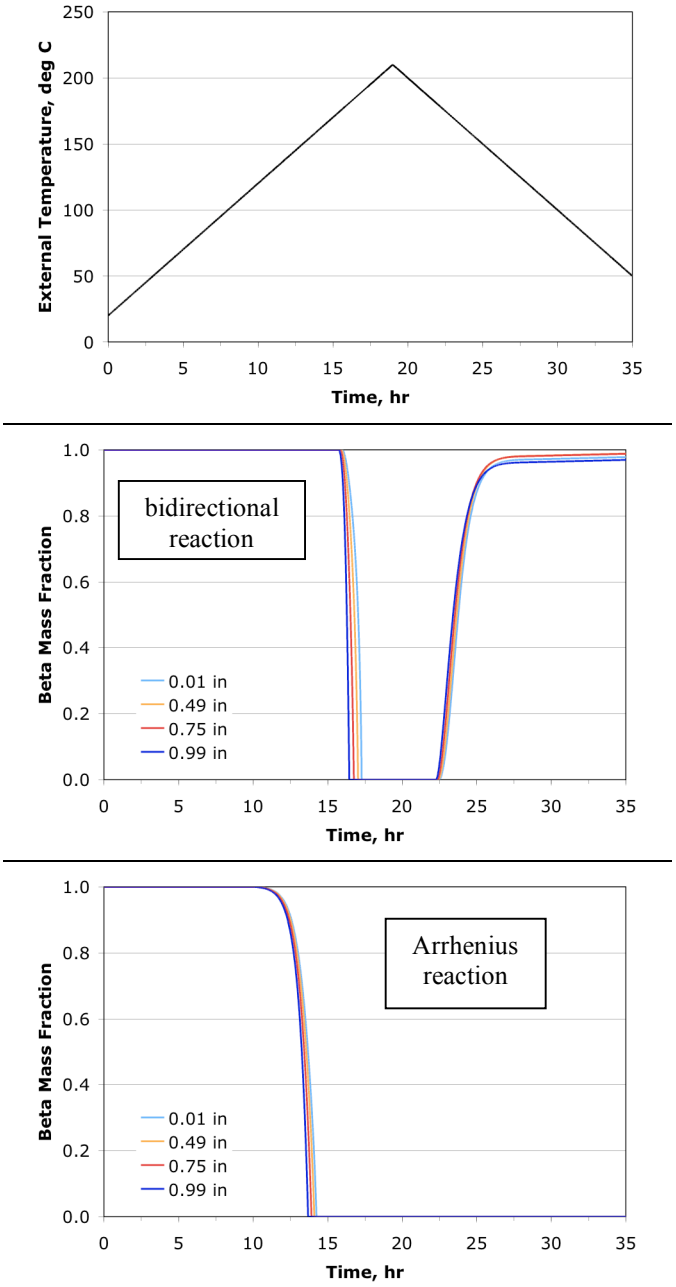

FIGURE 4. External temperature and beta phase mass fraction history curves at various radial positions for a 2" diameter cylinder using a zero order bidirectional or Arrhenius reaction.

The bidirectional kinetics models are comprised of only bidirectional-type reactions. A general form of these models is now described:

- *Bidirectional kinetics models*: the models follow

$$\begin{aligned}
&\beta \xleftrightarrow{k_1} \delta \\
&\beta \xleftrightarrow{k_2} \beta' \\
&\beta' \xleftrightarrow{k_3} \delta \\
&\beta + \delta \xleftrightarrow{k_4} 2\delta
\end{aligned} \tag{13}$$

Here, betaprime is a pseudo component that might be considered as a subcritical nucleus intermediate between the beta and delta phases. This reaction sequence results in changes in mass concentration values as

$$\begin{aligned}
\frac{dN_\beta}{dt} &= -k_1\left(T,N_\beta\right) - k_2\left(T,N_\beta\right) - k_4\left(T,N_\beta,N_\delta\right) \\
\frac{dN_{\beta'}}{dt} &= +k_2\left(T,N_\beta\right) - k_3\left(T,N_{\beta'}\right) \\
\frac{dN_\delta}{dt} &= +k_1\left(T,N_\beta\right) + k_3\left(T,N_{\beta'}\right) + k_4\left(T,N_\beta,N_\delta\right)
\end{aligned} \tag{14}$$

where N_β, $N_{\beta'}$ and N_δ are the mass concentration values of β-HMX, β'-HMX, and δ-HMX, respectively, and k_1, k_2, k_3, and k_4 are the reaction rates,

$$\begin{aligned}
k_1\left(T,N_\beta\right) &= A_1^0 N_\beta \exp\left(-\frac{E_1^*}{RT}\right)\sinh\left(\Lambda_e^* - \frac{E_e^*}{RT}\right) \\
k_2\left(T,N_\beta\right) &= A_2^0 N_\beta \exp\left(-\frac{E_2^*}{RT}\right)\sinh\left(\Lambda_e^* - \frac{E_e^*}{RT}\right) \\
k_3\left(T,N_{\beta'}\right) &= A_3^0 N_{\beta'}^n \exp\left(-\frac{E_3^*}{RT}\right)\sinh\left(\Lambda_e^* - \frac{E_e^*}{RT}\right) \\
k_4\left(T,N_\beta,N_\delta\right) &= A_4^0 N_\beta N_\delta \exp\left(-\frac{E_4^*}{RT}\right)\sinh\left(\Lambda_e^* - \frac{E_e^*}{RT}\right)
\end{aligned} \tag{15}$$

where the parameters constant for all three models are

$$\begin{aligned}
E_1^* &= E_2^* = E_3^* = 77129 \,{}^{\text{cal}}\!/\!_{\text{mol}} \\
E_4^* &= 7000 \,{}^{\text{cal}}\!/\!_{\text{mol}} \\
E_e^* &= 2347.8 \,{}^{\text{cal}}\!/\!_{\text{mol}} \\
\Lambda_e^* &= 2.728
\end{aligned} \tag{16}$$

and where the nonzero value of some frequency factors and the exponent n in the reaction rate equation k_3 are dependent upon the specific kinetics model. Table 3 provides a summary of known and unknown values for each kinetics model. One can see that Model 1 is a two-material model (no betaprime phase), while Models 2 and 3 are three-material models.

TABLE 3. Known Values of Uncalibrated Bidirectional Kinetics Models.

Parameter	**Bidirectional kinetics model**		
	Model 1	*Model 2*	*Model 3*
A_1^0, s^{-1}	Unknown	0	0
A_2^0, s^{-1}	0	Unknown	Unknown
A_3^0, s^{-1}	0	Unknown	Unknown
A_4^0, s^{-1}	Unknown	Unknown	Unknown
n	N/A	1	2
Number of materials	2	3	3

A reversible kinetics model was also used for comparative purposes. This model consists of only Arrhenius-type kinetics, and it contains known parameters for all reactions.

- *Reversible kinetics model*: autocatalytic model by Henson et al. (2002), pressure dependencies ignored. This model is calibrated based on PBX-9501 experimental findings. The reaction follows

$$\begin{aligned} &\beta \xrightarrow{k_1} \delta \\ &\delta \xrightarrow{k_{-1}} \beta \\ &\beta + \delta \xrightarrow{k_2} 2\delta \\ &\beta + \delta \xrightarrow{k_{-2}} 2\beta \end{aligned} \tag{17}$$

which results in changes in mass concentration values as

$$\begin{aligned} \frac{dN_\beta}{dt} &= -k_1\left(T,N_\beta\right) - k_2\left(T,N_\beta,N_\delta\right) + k_{-1}\left(T,N_\delta\right) + k_{-2}\left(T,N_\beta,N_\delta\right) \\ \frac{dN_\delta}{dt} &= +k_1\left(T,N_\beta\right) + k_2\left(T,N_\beta,N_\delta\right) - k_{-1}\left(T,N_\delta\right) - k_{-2}\left(T,N_\beta,N_\delta\right) \end{aligned} \tag{18}$$

where N_β and N_δ are the mass concentration values of β-HMX and δ-HMX, respectively, and k_1, k_2, k_{-1},and k_{-2} are the reaction rates,

$$
\begin{aligned}
k_1\left(T,N_\beta\right) &= A_1^0 N_\beta \exp\left(-\frac{E_1^*}{RT}\right) \\
k_{-1}\left(T,N_\delta\right) &= A_{-1}^0 N_\delta \exp\left(-\frac{E_{-1}^*}{RT}\right) \\
k_2\left(T,N_\beta,N_\delta\right) &= A_2^0 N_\beta N_\delta \exp\left(-\frac{E_2^*}{RT}\right) \\
k_{-2}\left(T,N_\beta,N_\delta\right) &= A_{-2}^0 N_\beta N_\delta \exp\left(-\frac{E_{-2}^*}{RT}\right)
\end{aligned}
\tag{19}
$$

where the parameters used are

$$
\begin{aligned}
A_1^0 &= 2.923\times 10^{14}\,\mathrm{us}^{-1} \\
A_{-1}^0 &= 1.892\times 10^{13}\,\mathrm{us}^{-1} \\
A_2^0 &= 1.059\times 10^{3}\,\mathrm{us}^{-1} \\
A_{-2}^0 &= 6.855\times 10^{1}\,\mathrm{us}^{-1} \\
E_1^* &= 49{,}638\,\mathrm{cal}/\mathrm{mol} \\
E_{-1}^* &= 47{,}296\,\mathrm{cal}/\mathrm{mol} \\
E_2^* &= 19{,}048\,\mathrm{cal}/\mathrm{mol} \\
E_{-2}^* &= 16{,}706\,\mathrm{cal}/\mathrm{mol}
\end{aligned}
\tag{20}
$$

Calibration of Bidirectional Kinetics Models

The unknown frequency factors in Table 3 were calibrated using ALE2D simulations of the aforementioned experimental setup scenarios. Known data from the experimental setup scenarios that were used for calibration are:

- 165°C XRD: the 50% conversion rate is known to occur at approximately three hours, and the duration of the transition is approximately three hours.
- SITI: the temperature profiles along the center plane at various radii are provided in a paper by Kaneshige et al. (2002). The calibration is based on qualitatively matching the time-temperature curves.

During the calibration, it was desired to limit the amount of betaprime produced in Models 2 and 3. This was achieved by reducing the frequency factors of the betaprime

production (k_2) by a factor of 100 compared to the factors for the conversion of betaprime to delta (k_3):

$$A_3^0 = 100 A_2^0 \tag{21}$$

It must be stressed that the calibration done in this study involved many assumptions to minimize degrees of freedom in parameter iteration. The goal of this study was to show that such an effort in parameter calibration is feasible to provide reasonable qualitative results when compared to experimental data. Tables 4a and 4b show the same values as Table 3 with the calibrated parameters using the 165°C XRD and SITI bases, respectively. The tables show that value of the frequency factor A_4^0 is approximately an order of magnitude larger for the SITI calibration compared to the 165°C XRD calibration. In addition, in Models 1 and 2, the other frequency factors are independent of the calibration method.

TABLE 4a. Calibrated Values of Bidirectional Kinetics Models Based on the 165°C XRD Experiments.

Parameter	**Bidirectional kinetics model**		
	Model 1	*Model 2*	*Model 3*
A_1^0, s^{-1}	1.0×10^{34}	0	0
A_2^0, s^{-1}	0	4.2×10^{33}	1.0×10^{32}
A_3^0, s^{-1}	0	4.2×10^{35}	1.0×10^{34}
A_4^0, s^{-1}	3.0×10^{1}	5.0×10^{1}	1.3×10^{2}
n	N/A	1	2
Number of materials	2	3	3

TABLE 4b. Calibrated Values of Bidirectional Kinetics Models Based on the SITI Experiment.

Parameter	**Bidirectional kinetics model**		
	Model 1	*Model 2*	*Model 3*
A_1^0, s^{-1}	1.0×10^{34}	0	0
A_2^0, s^{-1}	0	4.2×10^{33}	1.0×10^{32}
A_3^0, s^{-1}	0	4.2×10^{35}	1.0×10^{34}
A_4^0, s^{-1}	4.0×10^{2}	8.5×10^{2}	5.0×10^{2}
n	N/A	1	2
Number of materials	2	3	3

Application of Kinetics Models to Various Experimental Setup Scenarios

165°C XRD scenario

The four kinetics models were used to analyze the beta-delta phase transition for the four aforementioned experimental setup scenarios. Table 5 provides values of the 50% delta formation time and the 1%-99% delta formation duration for the 165°C XRD setup, and Figures 5 through 11 show time history curves of the internal temperature and the mass fraction of the various phases during the transition. The table and figures clearly show the discrepancy in delta formation time when the 165°C XRD setup is used to calibrate the kinetics versus the SITI setup. Although the fastest kinetics occur with the Reversible LANL model, all bidirectional models using parameters calibrated via the SITI setup contain delta formation times about a factor of 10 faster than desired for the 165°C XRD experiment. The table also shows that of the three bidirectional kinetics models whose parameters were calibrated based on the 165°C XRD scenario, the delta formation duration tends to decrease with the model's complexity (i.e. Model 3 yields the smallest duration).

TABLE 5: 50% Delta Formation Time and 1%-99% Delta Formation Duration for 165°C XRD Experimental Setup Scenario

Kinetics Model	Scenario for Calibration of Parameters	50% Delta Formation Time, hr	1%-99% Delta Formation Duration, hr
Reversible LANL	N/A	0.06	0.09
Bidirectional Model 1	165°C XRD	3.0	4.4
	SITI	0.31	0.35
Bidirectional Model 2	165°C XRD	3.0	3.8
	SITI	0.20	0.16
Bidirectional Model 3	165°C XRD	2.9	1.0
	SITI	0.29	0.21

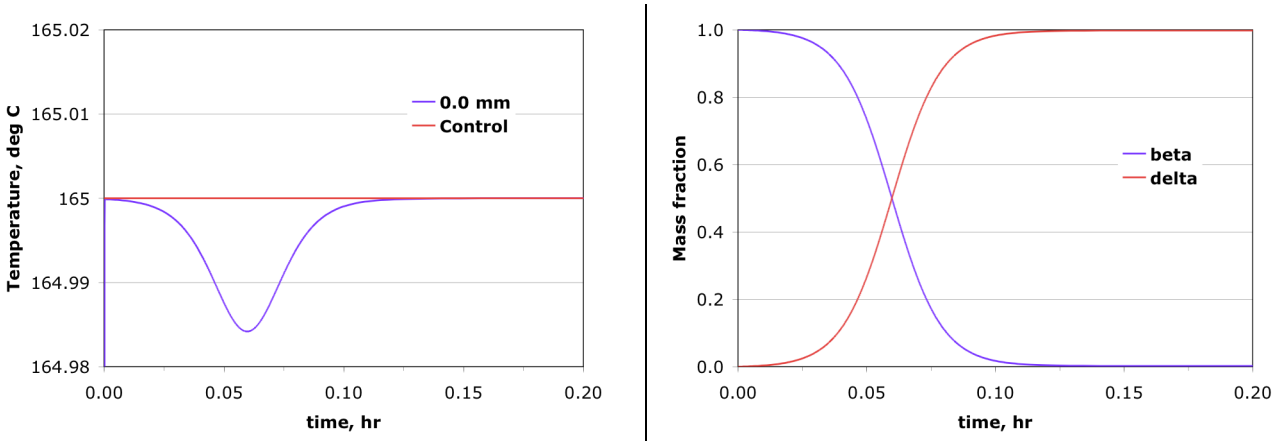

FIGURE 5. Centerline temperature and phase mass fraction history curves using the reversible LANL kinetics model for the 165°C XRD experimental scenario.

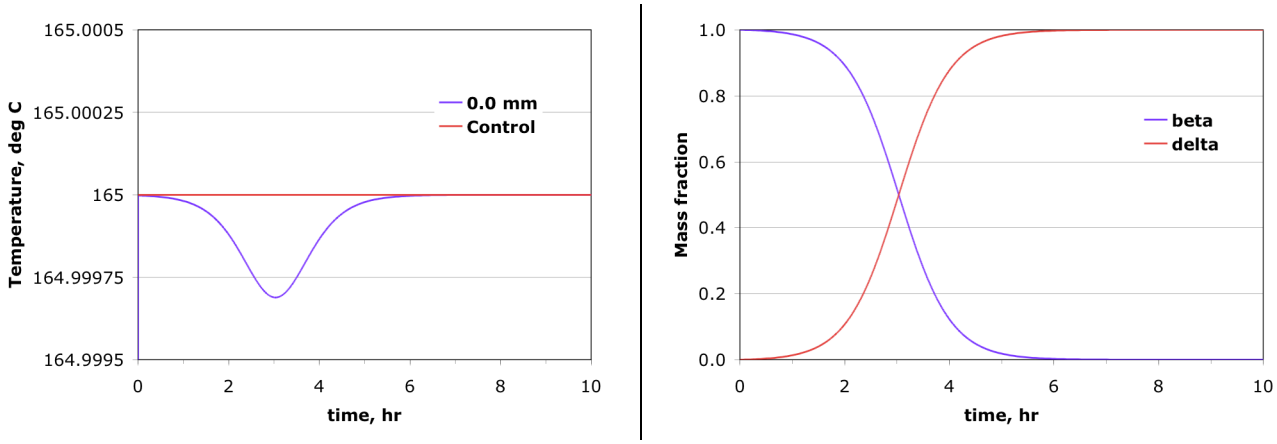

FIGURE 6. Centerline temperature and phase mass fraction history curves of bidirectional kinetics Model 1 for the 165°C XRD experimental scenario. Kinetic parameters were calibrated using this scenario.

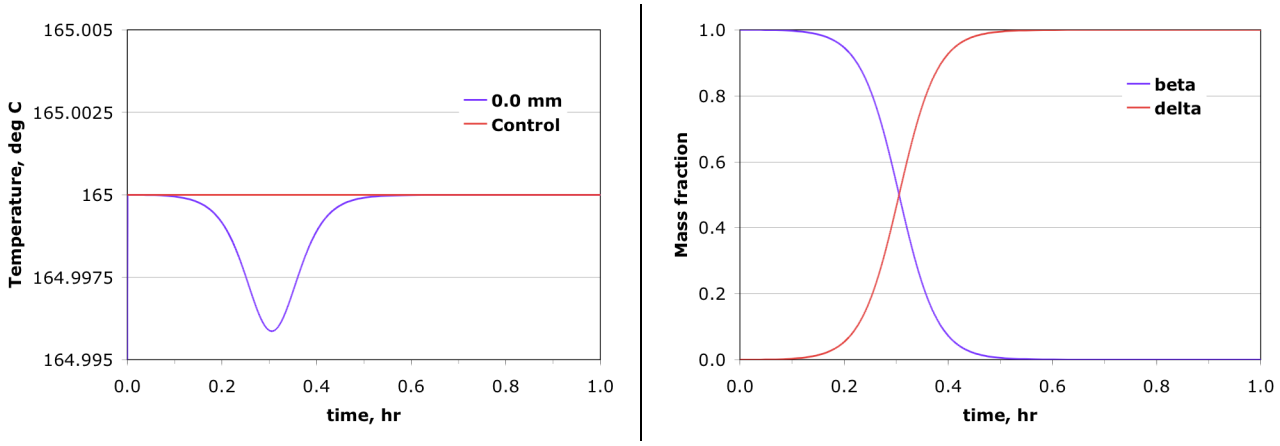

FIGURE 7. Centerline temperature and phase mass fraction history curves of bidirectional kinetics Model 1 for the 165°C XRD experimental scenario. Kinetic parameters were calibrated using the SITI scenario.

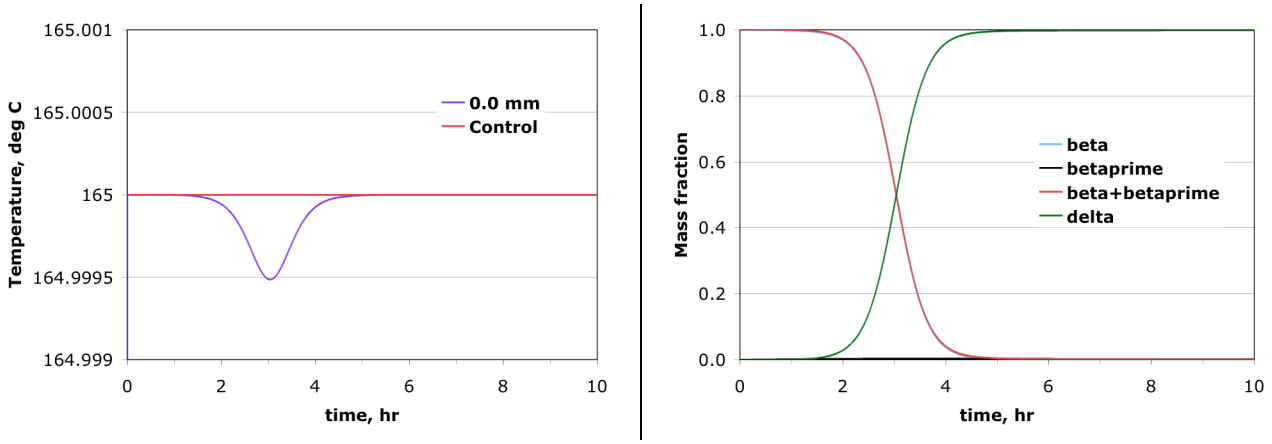

FIGURE 8. Centerline temperature and phase mass fraction history curves of bidirectional kinetics Model 2 for the 165°C XRD experimental scenario. Kinetic parameters were calibrated using this scenario.

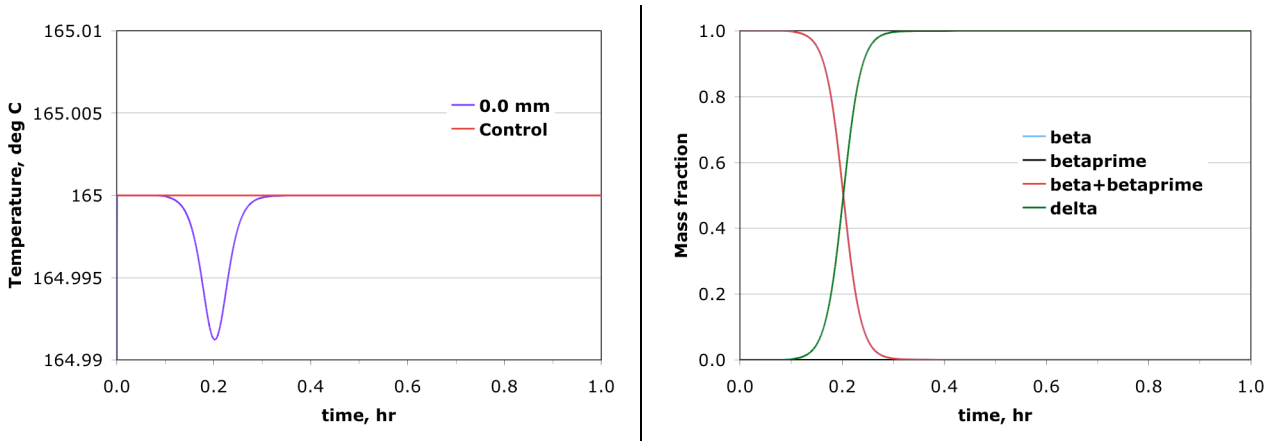

FIGURE 9. Centerline temperature and phase mass fraction history curves of bidirectional kinetics Model 2 for the 165°C XRD experimental scenario. Kinetic parameters were calibrated using the SITI scenario.

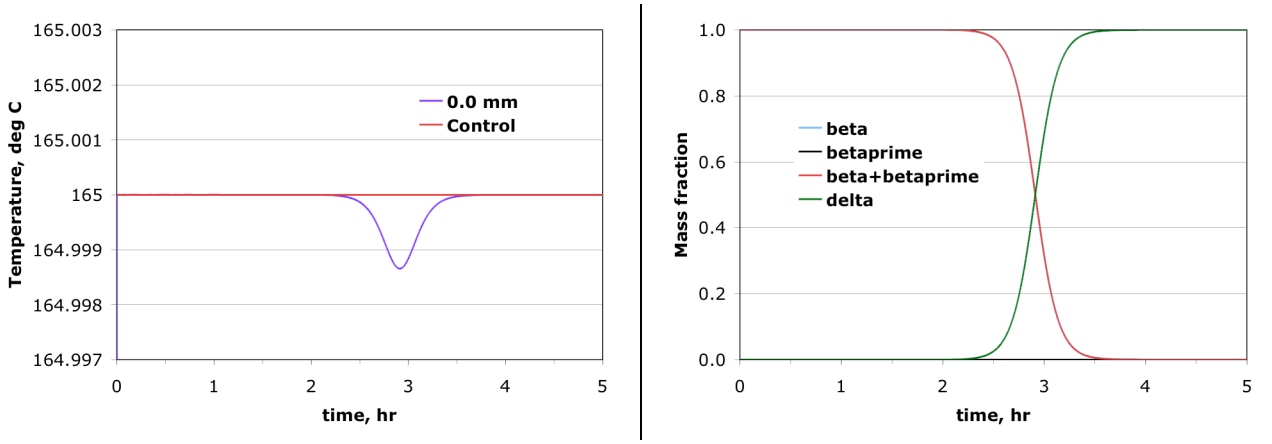

FIGURE 10. Centerline temperature and phase mass fraction history curves of bidirectional kinetics Model 3 for the 165°C XRD experimental scenario. Kinetic parameters were calibrated using this scenario.

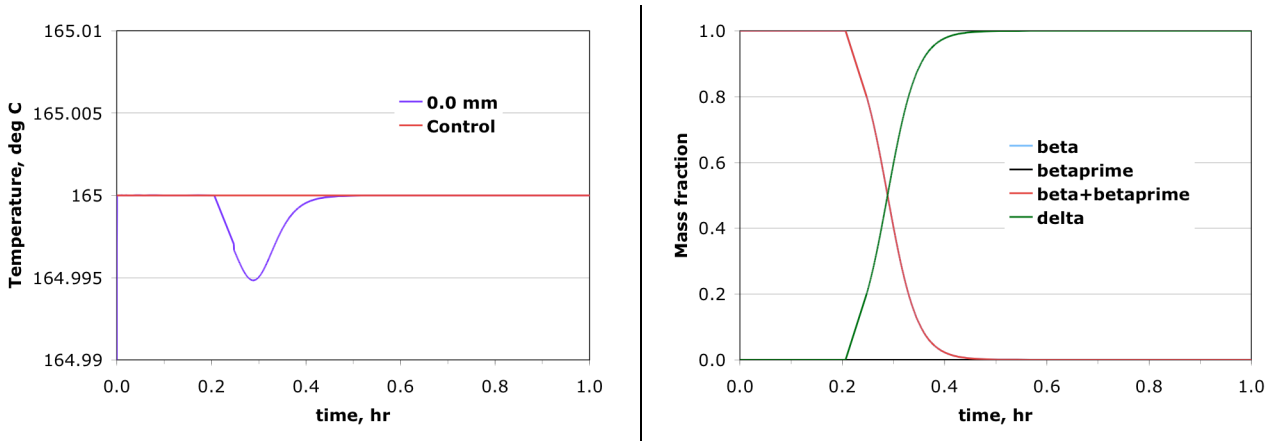

FIGURE 11. Centerline temperature and phase mass fraction history curves of bidirectional kinetics Model 3 for the 165°C XRD experimental scenario. Kinetic parameters were calibrated using the SITI scenario.

175°C XRD scenario

Zaug's 175°C XRD experiment was also used for comparison of the various kinetics models and their methods of calibration. The conversion is 100% complete at the 17-minute resolution of the XRD measurement, and SHG generation is at 80% of its ultimate value at 5 minutes. Table 6 shows the values of the 50% delta formation time and 1%-99% delta formation for the various kinetics models, and Figures 12 through 18 provide time history curves of the centerline temperature and mass fractions. The Reversible LANL model has a substantially smaller 50% delta formation time and 1%-99% delta formation duration than any of the bidirectional kinetics models, but both the LANL and SITI-scenario models agree with the data within the limited time resolution. The kinetic parameters calibrated on the 165°C XRD data predict a slower transition at 175°C than is observed. The conversion times using parameters calibrated via the SITI scenario are generally an order of magnitude faster than those calibrated using the 165°C data, which is consistent with Table 5.

TABLE 6: 50% Delta Formation Time and 1%-99% Delta Formation Duration for 175°C XRD Experimental Setup Scenario

Kinetics Model	Scenario for Calibration of Parameters	50% Delta Formation Time, min	1%-99% Delta Formation Duration, min
Reversible LANL	N/A	1.0	1.5
Model 1	165°C XRD	60.1	103.3
	SITI	6.6	8.1
Model 2	165°C XRD	57.8	68.6
	SITI	4.7	3.9
Model 3	165°C XRD	37.9	25.1
	SITI	6.5	4.9

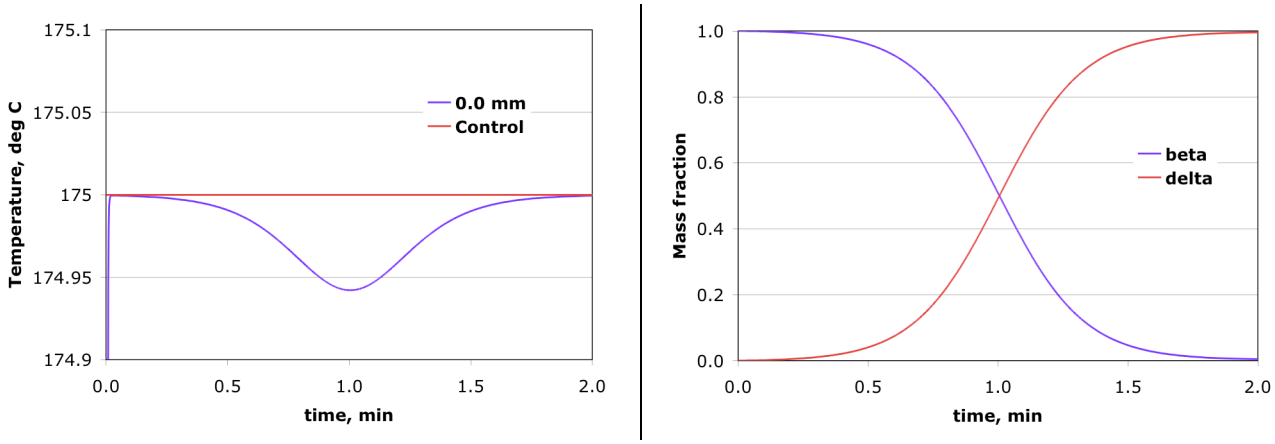

FIGURE 12. Centerline temperature and phase mass fraction history curves using the reversible LANL kinetics model for the 175°C XRD scenario.

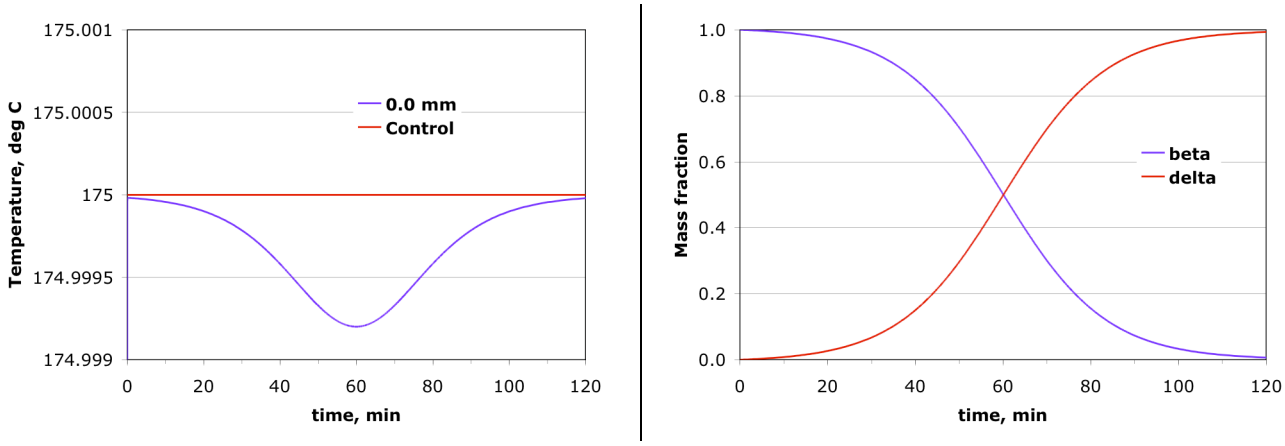

FIGURE 13. Centerline temperature and phase mass fraction history curves of bidirectional kinetics Model 1 for the 175°C XRD experimental scenario. Kinetic parameters were calibrated using the 165°C XRD scenario.

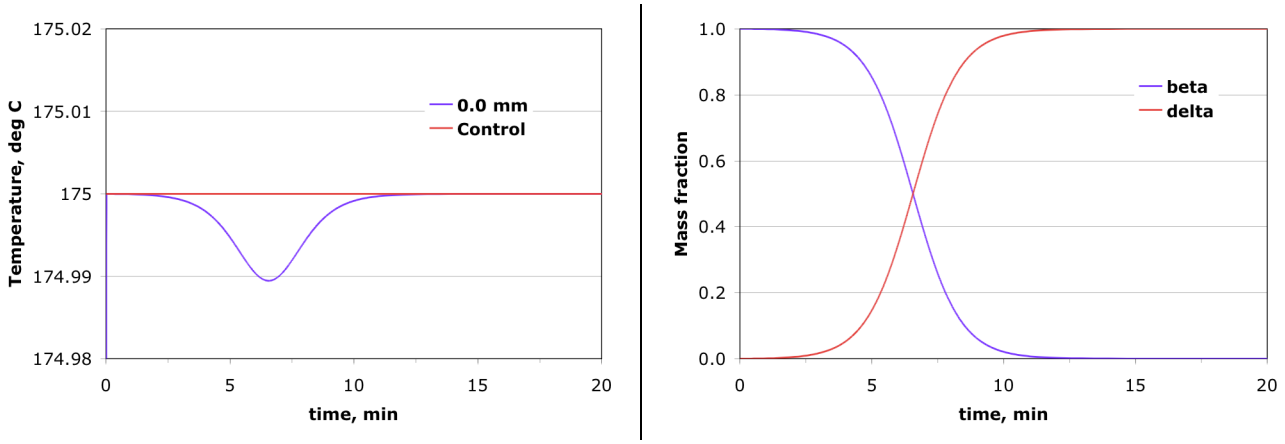

FIGURE 14. Centerline temperature and phase mass fraction history curves of bidirectional kinetics Model 1 for the 175°C XRD experimental scenario. Kinetic parameters were calibrated using the SITI scenario.

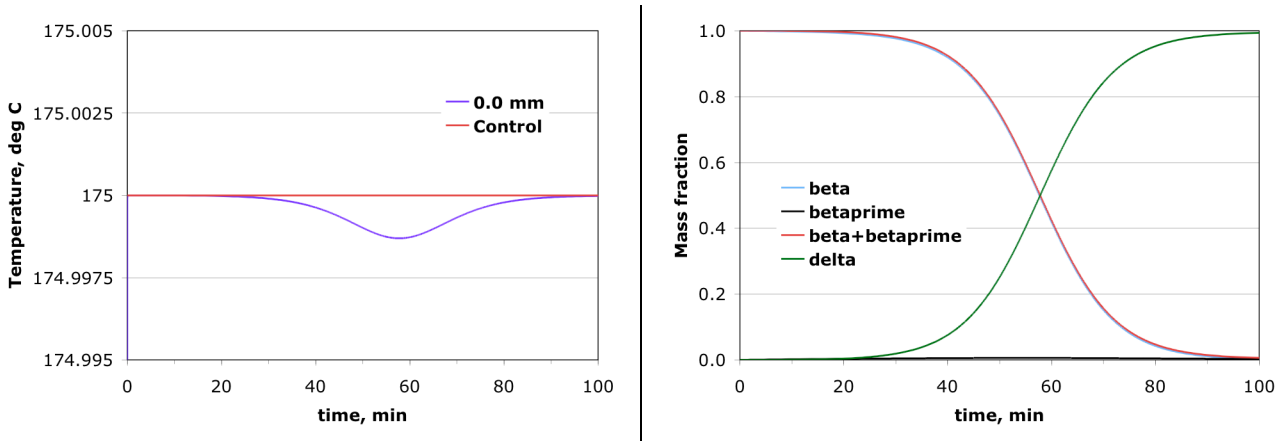

FIGURE 15. Centerline temperature and phase mass fraction history curves of bidirectional kinetics Model 2 for the 175°C XRD experimental scenario. Kinetic parameters were calibrated using the 165°C XRD scenario.

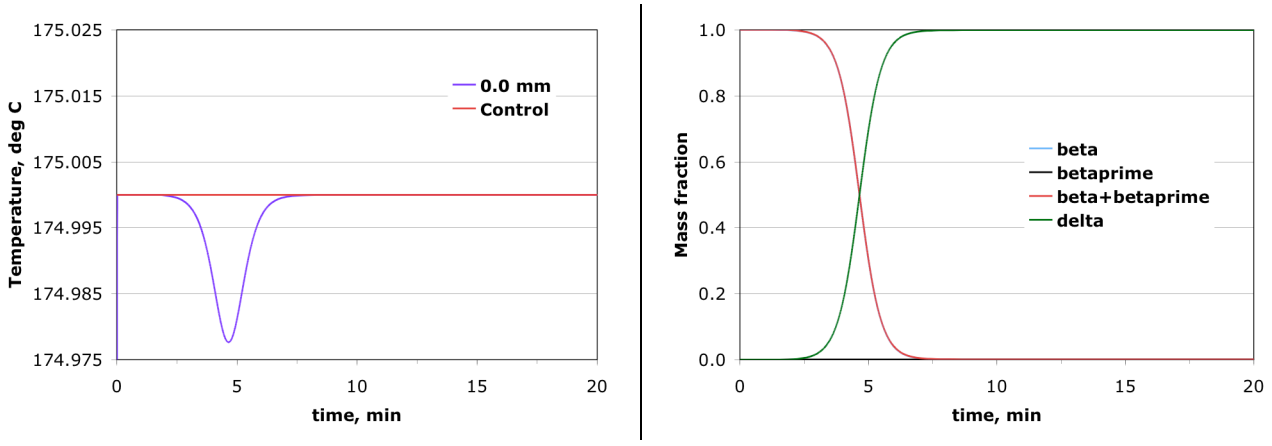

FIGURE 16. Centerline temperature and phase mass fraction history curves of bidirectional kinetics Model 2 for the 175°C XRD experimental scenario. Kinetic parameters were calibrated using the SITI scenario.

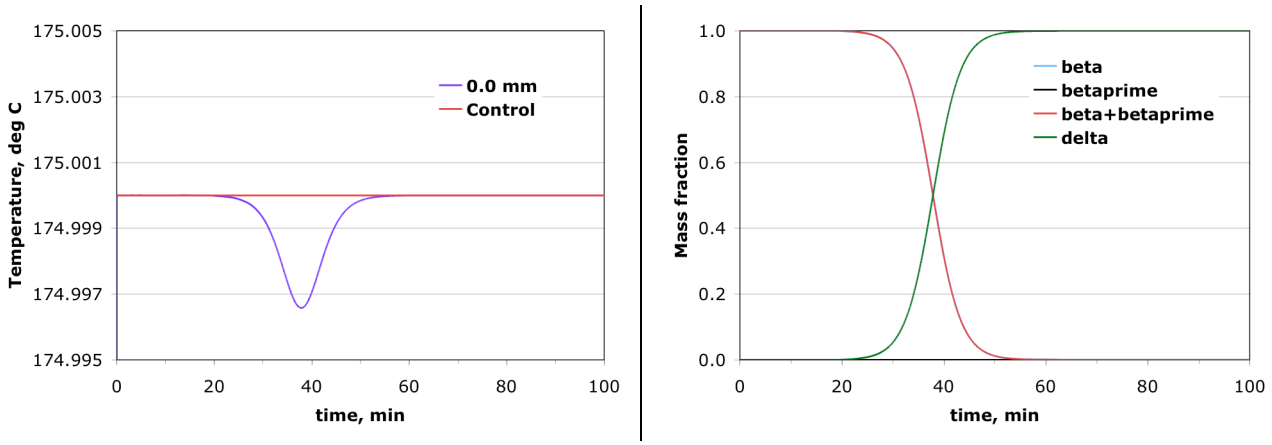

FIGURE 17. Centerline temperature and phase mass fraction history curves of bidirectional kinetics Model 3 for the 175°C XRD experimental scenario. Kinetic parameters were calibrated using the 165°C XRD scenario.

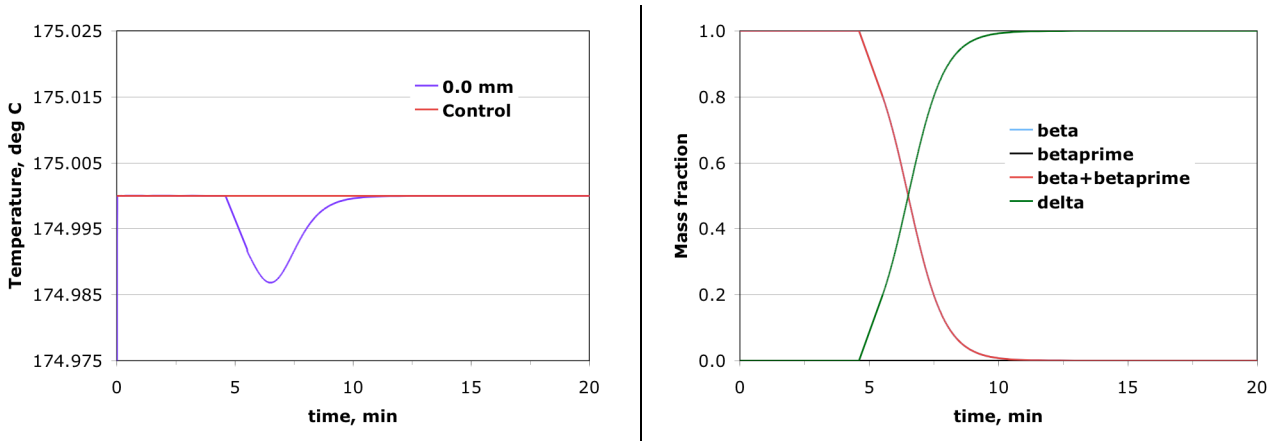

FIGURE 18. Centerline temperature and phase mass fraction history curves of bidirectional kinetics Model 3 for the 175°C XRD experimental scenario. Kinetic parameters were calibrated using the SITI scenario.

SITI scenario

Results by Kaneshige et. al. (2002) in Figure 19 show that the temperature history curves at various radii display a drop at 30-35 minutes, which is evidence of the endothermic beta-delta transition. The temperature then nearly recovers to the external temperature of 192°C at approximately 40 minutes. In this study, results for the SITI scenario are provided in Table 7 and Figures 20 through 26. The table shows the values of the 50% delta formation time for each of the kinetics models as well as the time at which the centerline temperature reaches 190°C. Table 7 shows these two values for the various kinetics, and Figures 20 through 26 provide time history curves of the centerline temperature and mass fractions. Table 7 shows that the time for the centerline temperature to reach 190°C is approximately 7 minutes longer for the 165°C models, which approximately corresponds to the transition time. Also, the 50% delta formation time using the Reversible LANL model agrees with the bidirectional kinetics whose parameters were calibrated using the SITI scenario. In contrast, the 50% delta formation time using parameters calibrated via the SITI scenario are approximately three times faster than those using the 165°C scenario, which is consistent with Table 5. The temperature histories for the various model scenarios show good qualitative agreement between experimental results and simulation results using the Reversible LANL model, which is expected since both the experimental results and this model are based on PBX-9501.

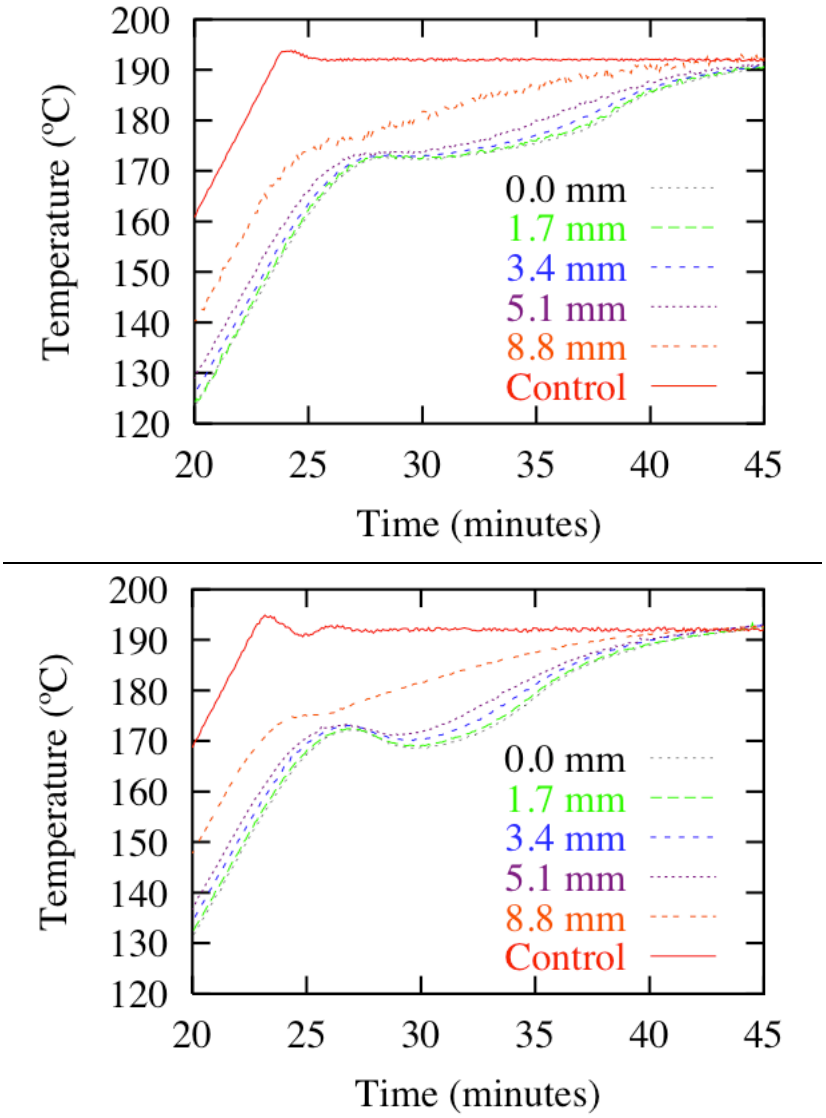

FIGURE 19. Experimental data by Kaneshige et al. (2002) of SITI experiment of PBX-9501. Top figure has 9.6% expansion volume, and bottom figure has 13.8% expansion volume (Reproduced with author's permission).

TABLE 7: 50% Delta Formation Time at Centerline and 190°C Centerline Temperature Time for SITI Experimental Setup Scenario

Kinetics Model	Scenario for Calibration of Parameters	50% Delta Formation Time at Centerline, min	190°C Centerline Temperature Time, min
Reversible LANL	N/A	27.7	34.6
Model 1	165°C XRD	85.8	32.6
	SITI	32.0	39.7
Model 2	165°C XRD	84.1	33.6
	SITI	31.1	38.0
Model 3	165°C XRD	49.1	33.6
	SITI	31.0	39.8

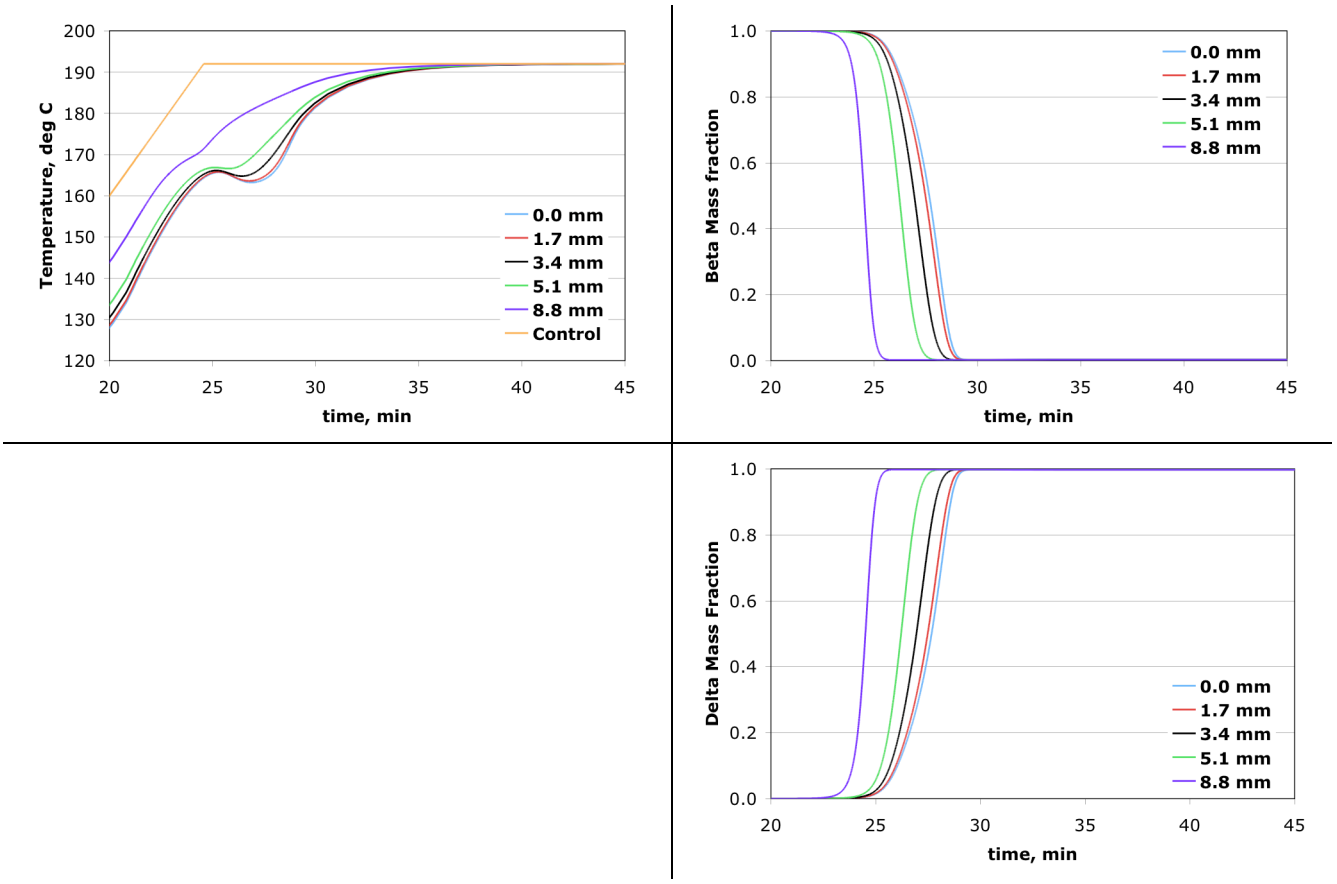

FIGURE 20. Temperature and phase mass fraction history curves as a function of radial position for the SITI experimental scenario using the reversible LANL kinetics model.

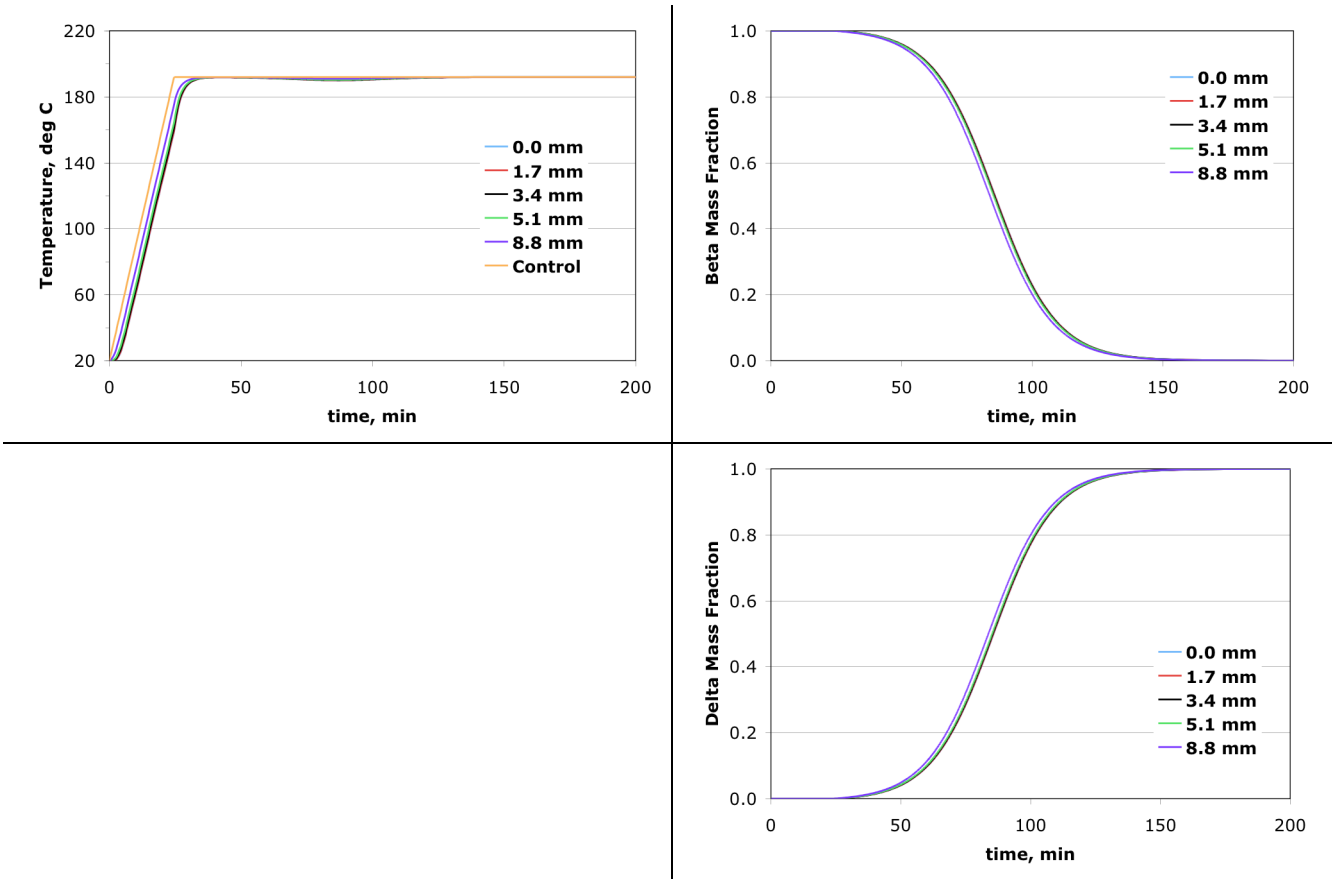

FIGURE 21. Temperature and phase mass fraction history curves as a function of radial position for the SITI experimental scenario using bidirectional kinetics Model 1. Kinetic parameters were calibrated using the 165°C XRD scenario.

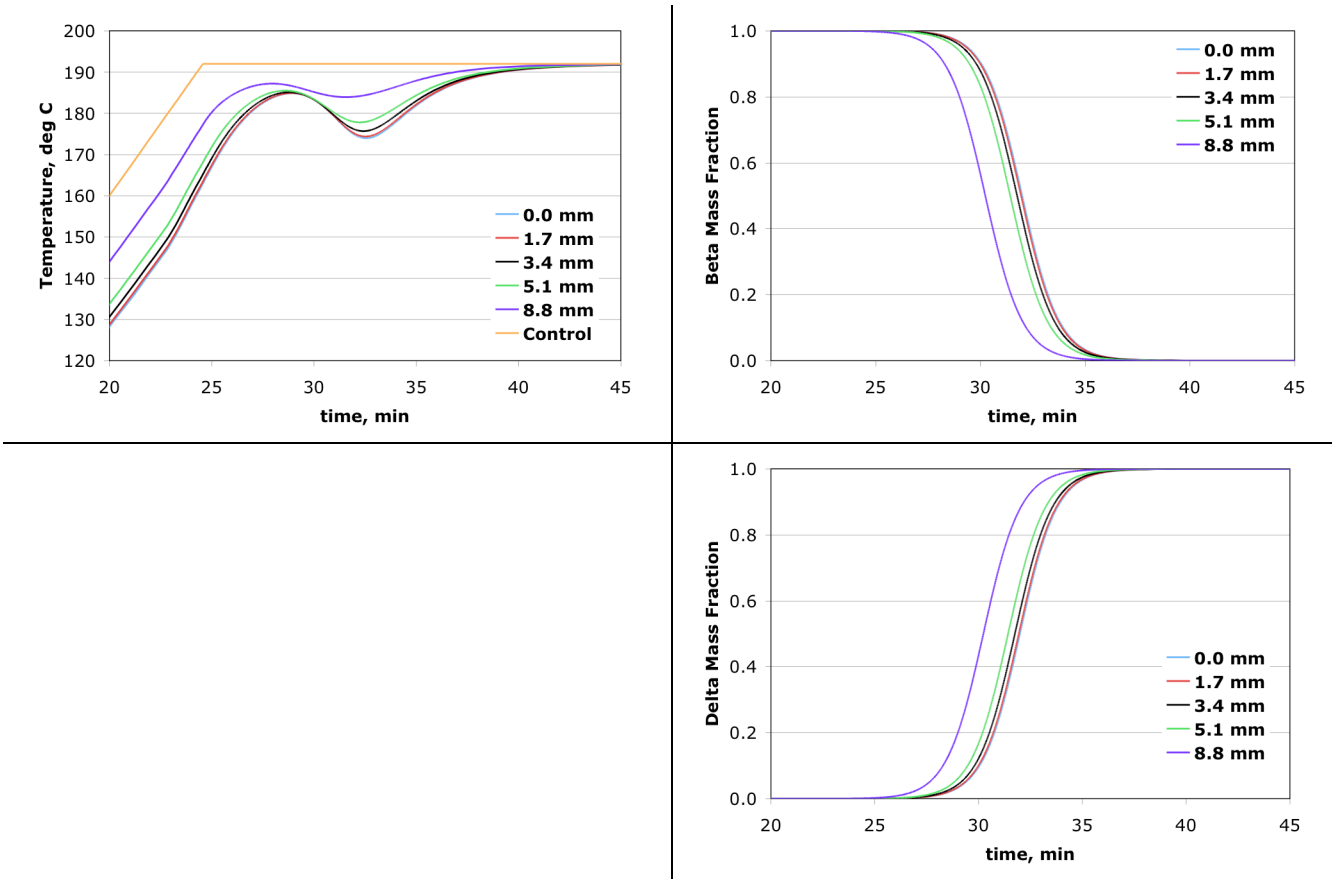

FIGURE 22. Temperature and phase mass fraction history curves as a function of radial position for the SITI experimental scenario using bidirectional kinetics Model 1. Kinetic parameters were calibrated using this scenario.

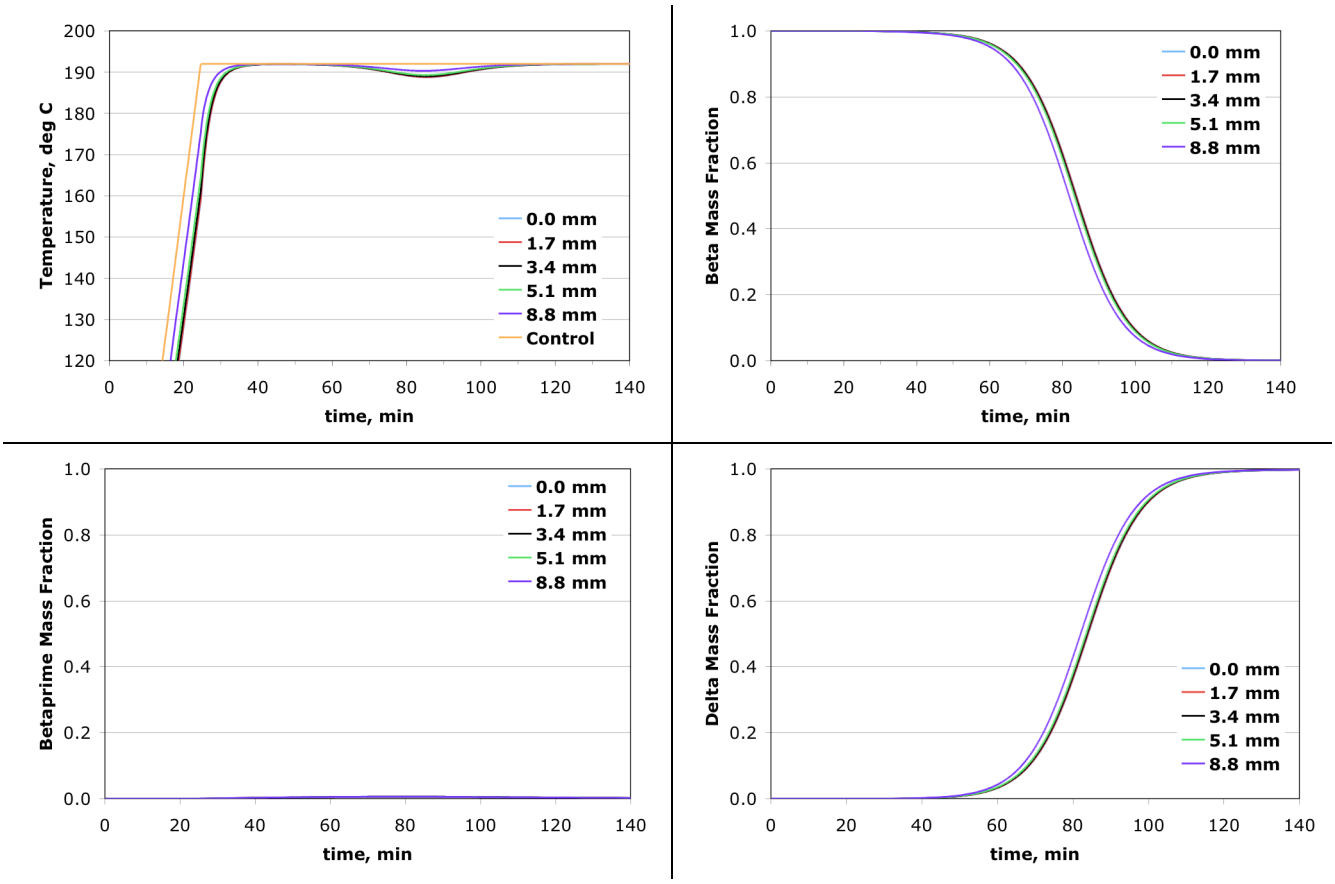

FIGURE 23. Temperature and phase mass fraction history curves as a function of radial position for the SITI experimental scenario using bidirectional kinetics Model 2. Kinetic parameters were calibrated using the 165°C XRD scenario.

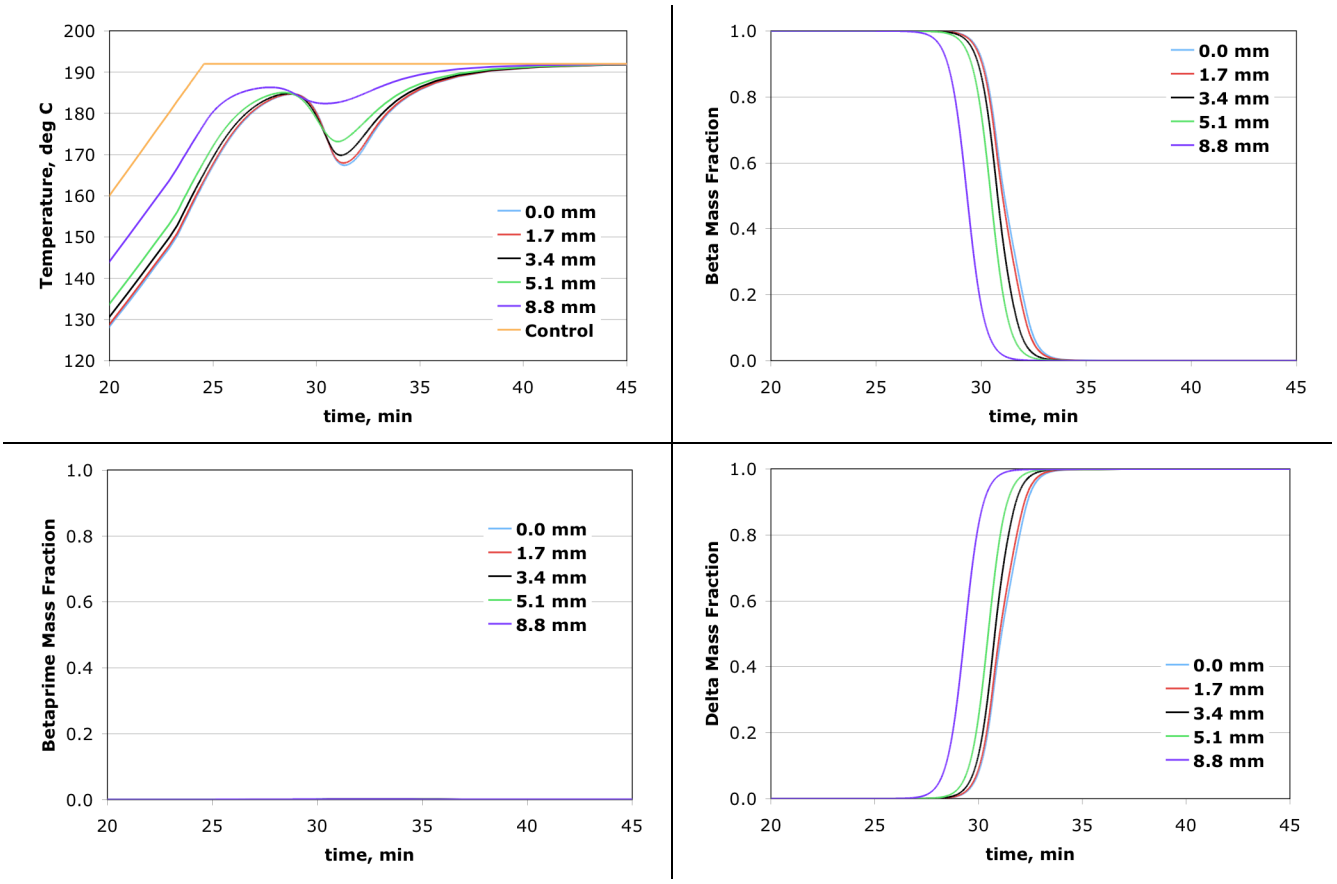

FIGURE 24. Temperature and phase mass fraction history curves as a function of radial position for the SITI experimental scenario using bidirectional kinetics Model 2. Kinetic parameters were calibrated using this scenario.

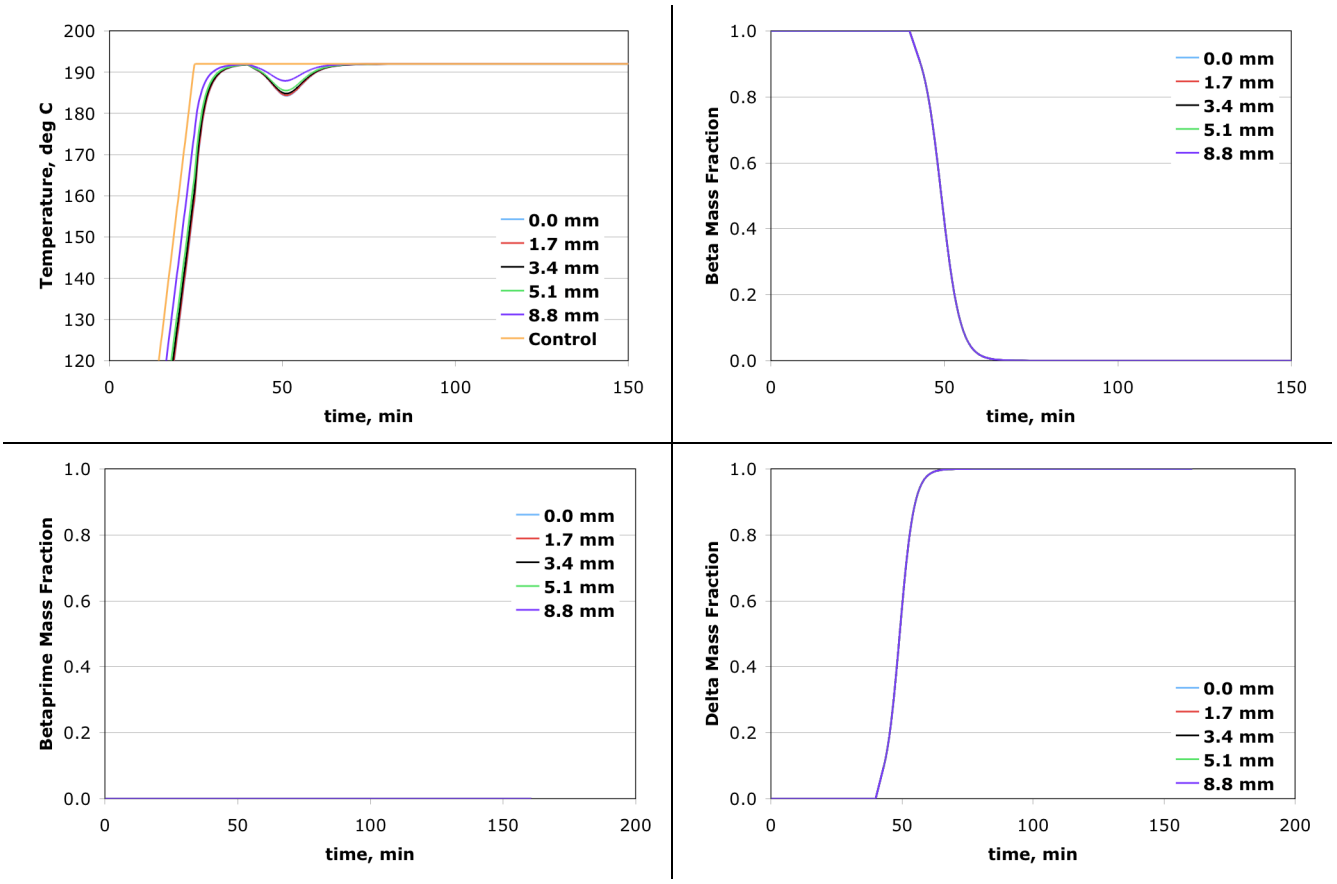

FIGURE 25. Temperature and phase mass fraction history curves as a function of radial position for the SITI experimental scenario using bidirectional kinetics Model 3. Kinetic parameters were calibrated using the 165°C XRD scenario.

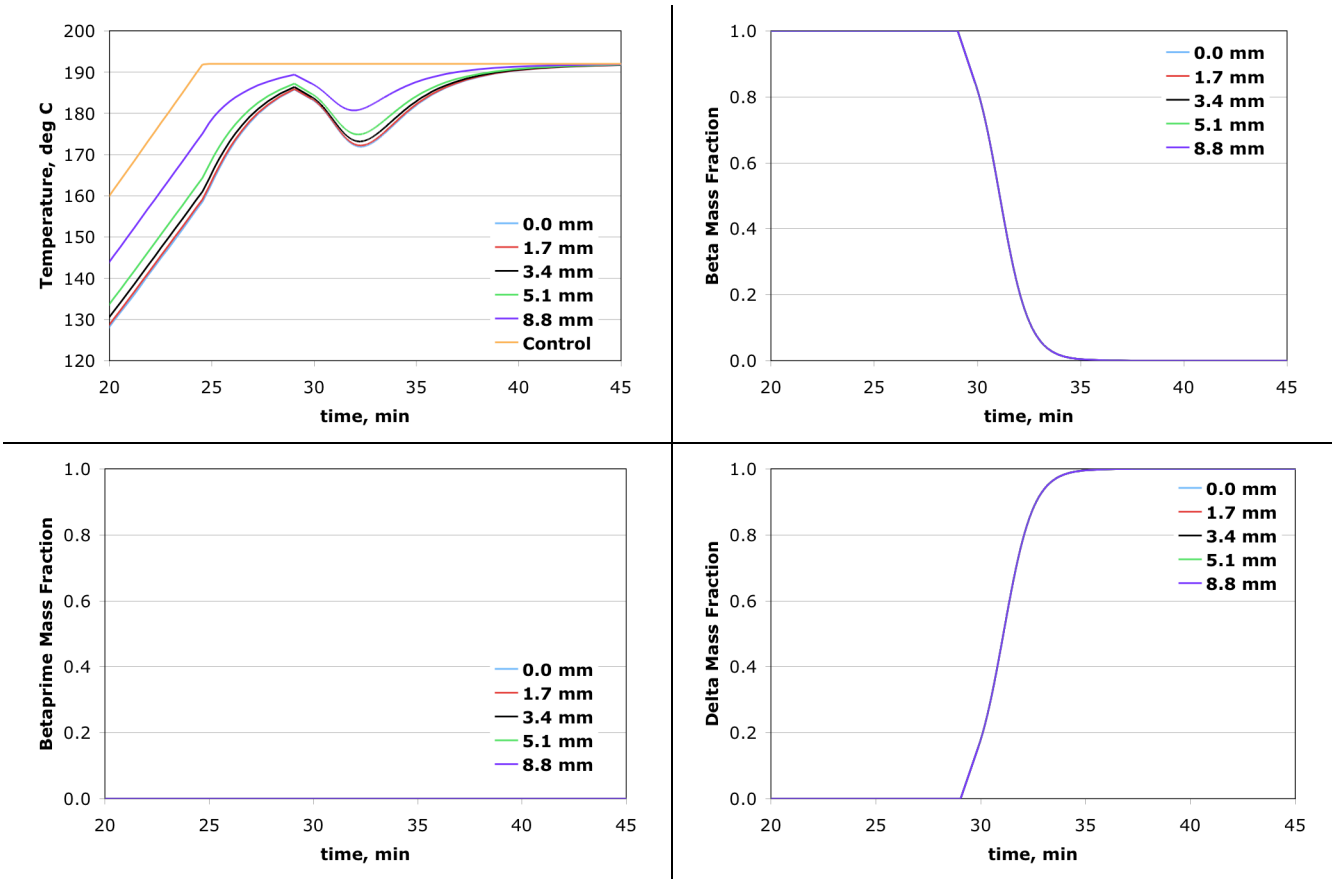

FIGURE 26. Temperature and phase mass fraction history curves as a function of radial position for the SITI experimental scenario using bidirectional kinetics Model 3. Kinetic parameters were calibrated using this scenario.

STEX scenario

Experimental results of the STEX scenario for PBX-9501 are shown in Figure 27. The temperature was slightly greater at the center than near the flanges at a given time due to a slightly greater heat input to the middle of the cylinder (midpoint between the two flanges), so it achieved a given temperature 5-10 minutes earlier than the ends of the HE. In the experimental data, the temporary temperature drop at 160°C to 164°C accompanies the endothermic phase transition. It is most evident in the middle centerline thermocouple (denoted "inside middle" in the figure), because it is the most removed from external thermal contact. This is consistent with results from the simulations shown in Figures 28 through 34. Table 8 below shows that the external temperature at 50% delta formation at the centerline is similar among all three bidirectional models with the common scenario for the calibration of their parameters. The scenarios with parameters calibrated using the SITI setup contain temperature values approximately 3-4°C lower than those calibrated using the 165°C XRD setup. The Reversible LANL model has the lowest 50% delta formation external temperature, which agrees with Tables 5 thru 7 in suggesting that it contains the fastest kinetics of any of the models. The experimental transition range of 160-164°C is most consistent with the LANL model and bidirectional models using parameters calibrated based on the SITI experimental data.

STEX experiments for HMX formulations using different binder content and particle sizes (LX-04 and LX-10) have also been performed, and they are similar to the transition times for PBX-9501 shown in Figure 27. Whereas Figure 27 shows an initial downturn in the centerline temperature at 160°C, the results for LX-04 and LX-10 show this downturn at 163-165°C and 155°C, respectively. Table 8 suggests that the STEX phase transition temperatures for the SITI-based and 165°C XRD-based bidirectional models are in reasonable agreement with the LX-04 results, while no model is consistent with the LX-10 result.

The precise reason for this variability is not known. One factor is that the presence of the nitroplasticizer is thought to accelerate the phase transition, which would explain why PBX-9501 transforms lower than LX-04. However, LX-10 uses the same Viton-A binder as in LX-04. Alternatively, Cady and Smith (1962) mention that RDX plays a role in accelerating the phase transition, although it is not completely clear whether that is only a kinetic effect or also a thermodynamic effect. Unfortunately, there have not been sufficient experiments with well-controlled and characterized properties (particle size, RDX content, and binder) to definitively determine the effects of these variables, and it was beyond the scope of the present report to determine them.

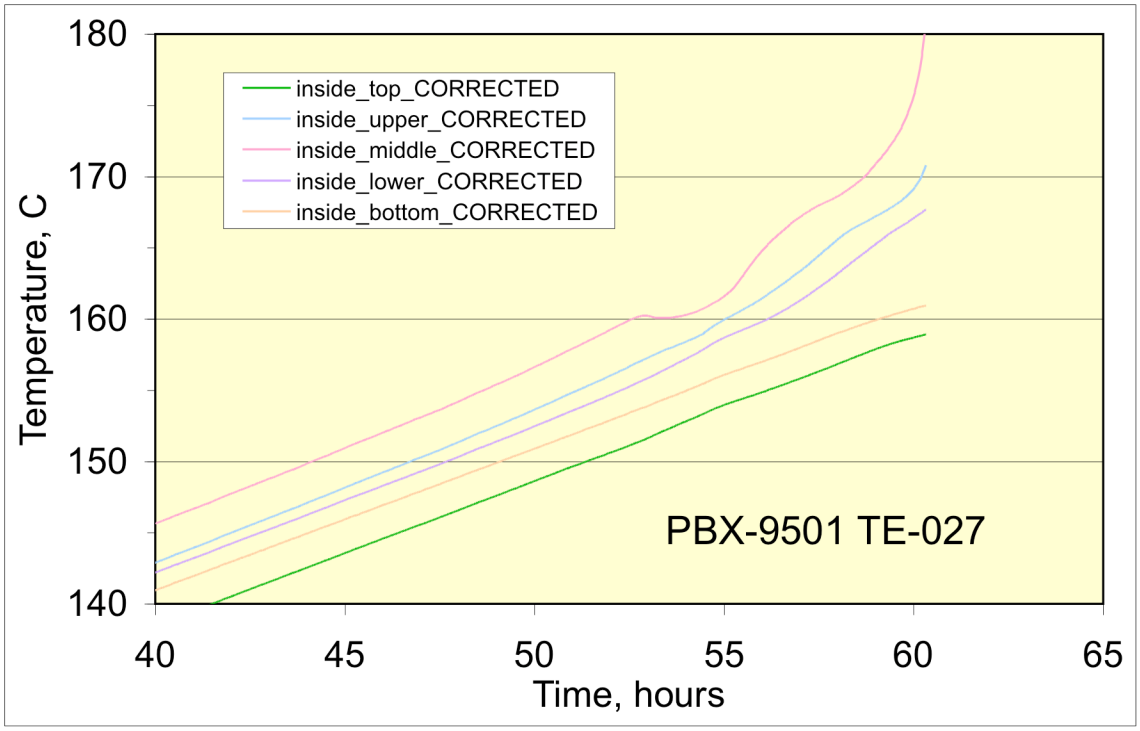

FIGURE 27. Experimental results from STEX experiment TE-027, which used PBX-9501.

TABLE 8: External Temperature at 50% Delta Formation for the STEX Experimental Setup Scenario

Kinetics Model	**Scenario for Calibration of Parameters**	**External Temperature at 50% Delta Formation at Centerline, deg C**
Reversible LANL	N/A	160.9
Model 1	165°C XRD	167.0
	SITI	162.4
Model 2	165°C XRD	166.8
	SITI	163.9
Model 3	165°C XRD	167.0
	SITI	164.8

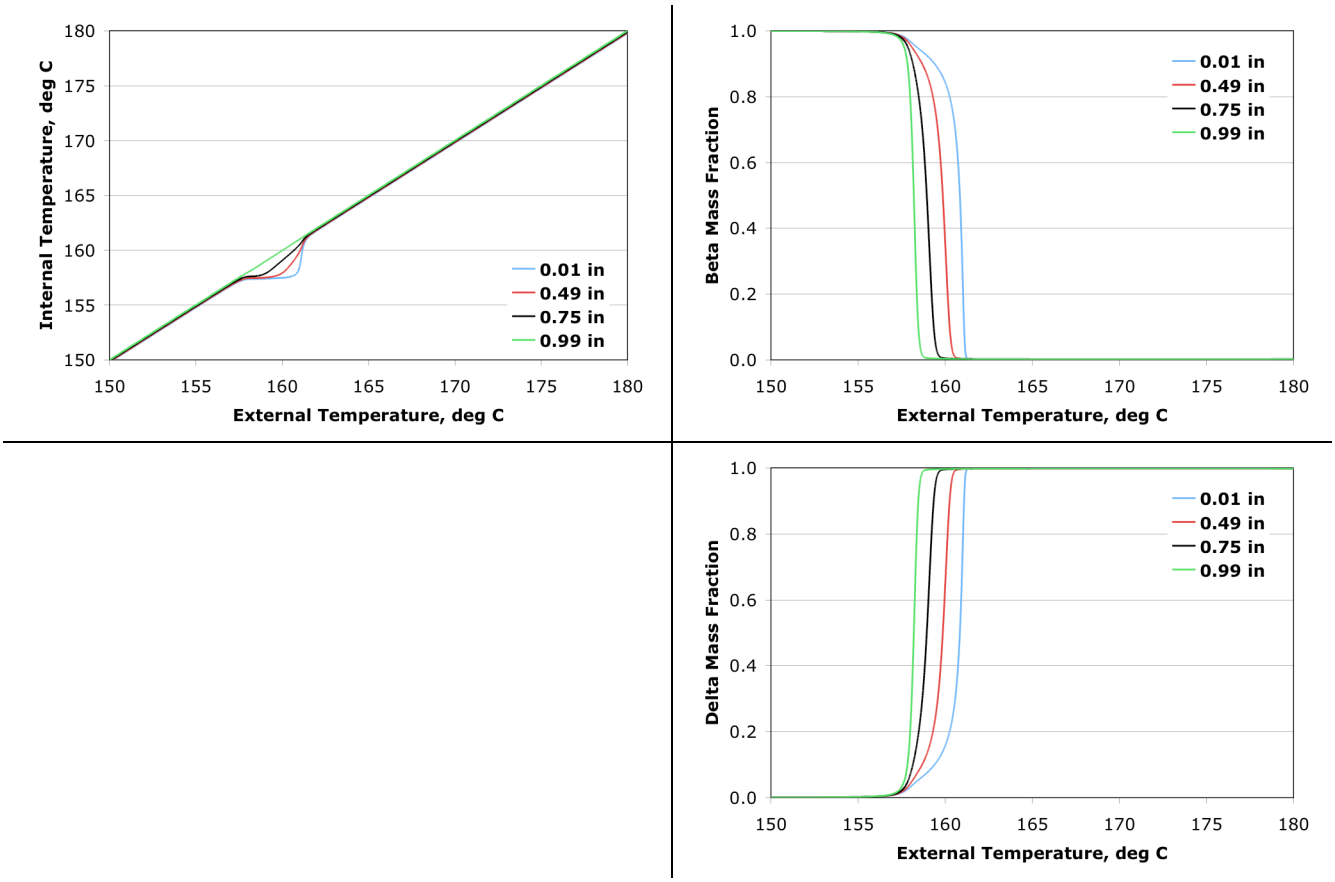

FIGURE 28. External temperature and phase mass fraction history curves as a function of radial position using the reversible LANL kinetics model for the STEX experimental scenario.

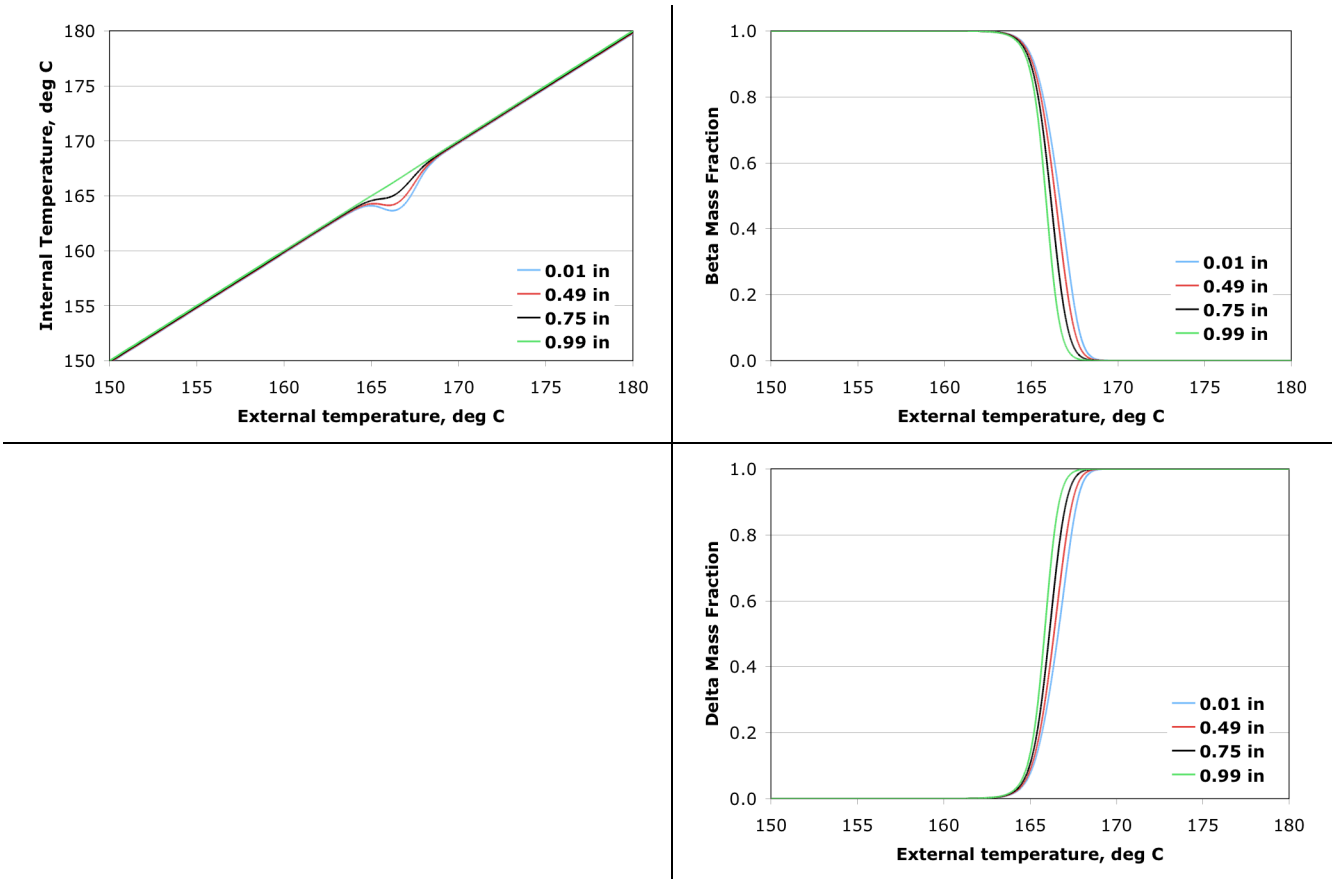

FIGURE 29. External temperature and phase mass fraction history curves as a function of radial position using bidirectional kinetics Model 1 for the STEX experimental scenario. Kinetic parameters were calibrated using the 165°C XRD scenario.

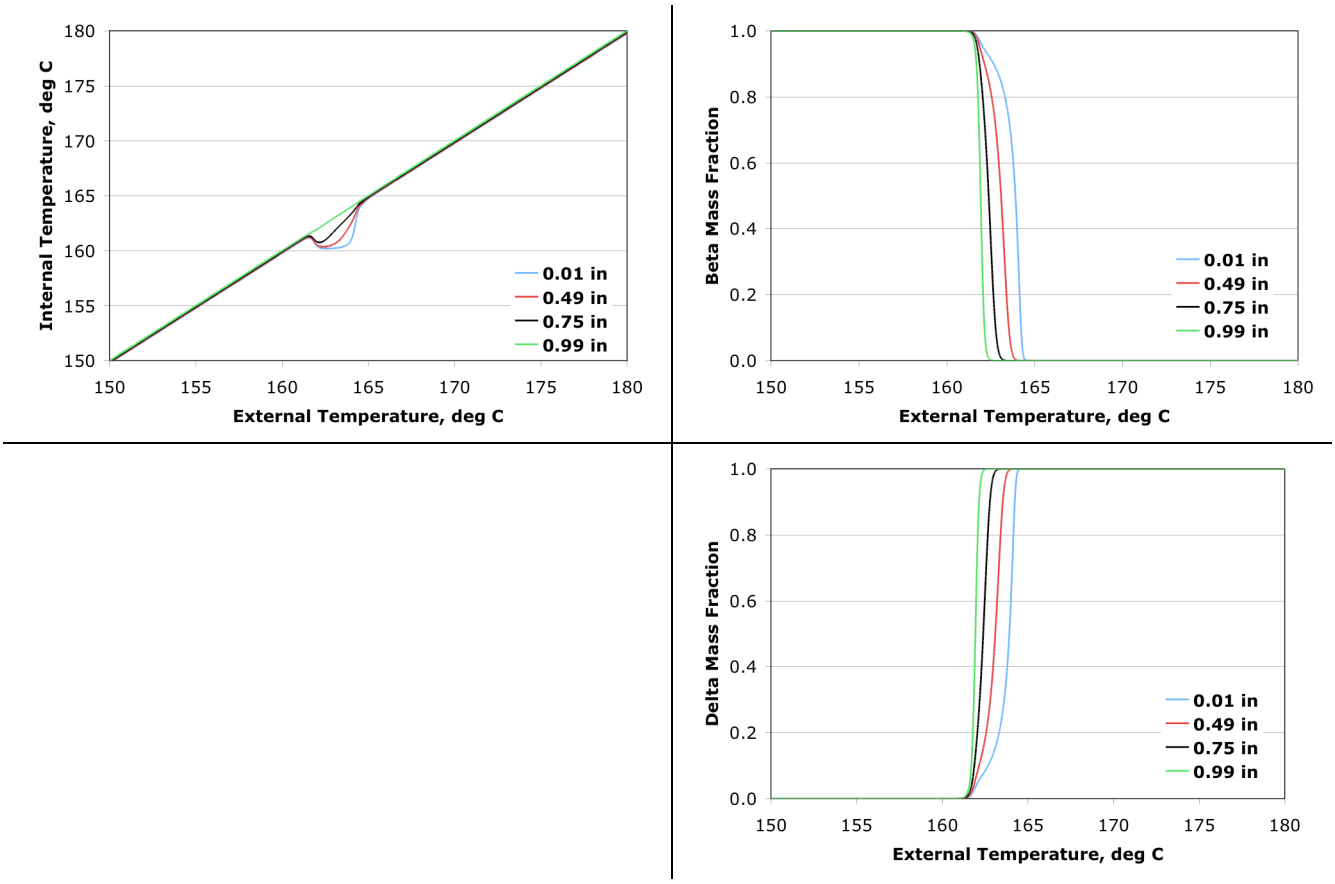

FIGURE 30. External temperature and phase mass fraction history curves as a function of radial position using bidirectional kinetics Model 1 for the STEX experimental scenario. Kinetic parameters were calibrated using the SITI scenario.

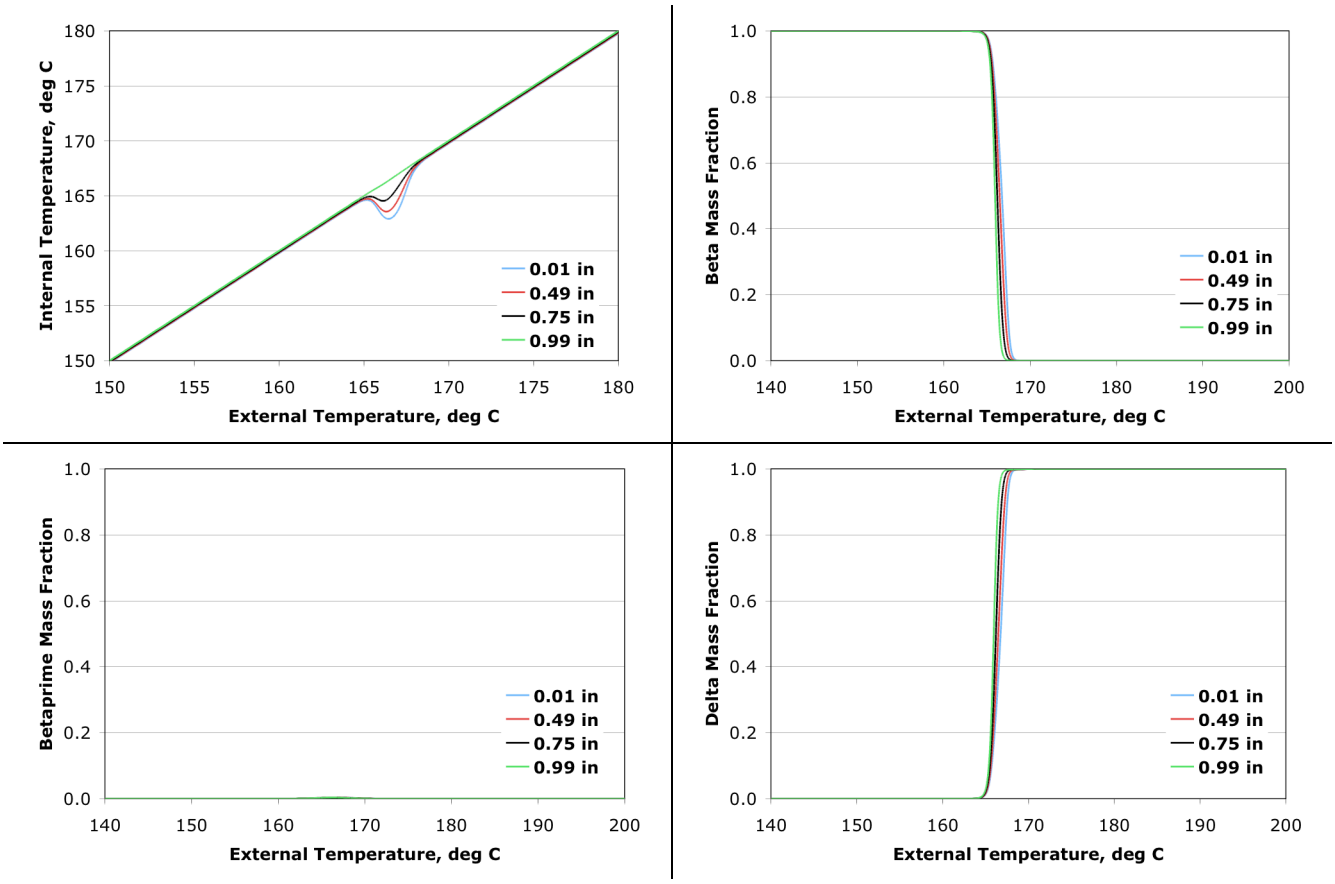

FIGURE 31. External temperature and phase mass fraction history curves as a function of radial position using bidirectional kinetics Model 2 for the STEX experimental scenario. Kinetic parameters were calibrated using the 165°C XRD scenario.

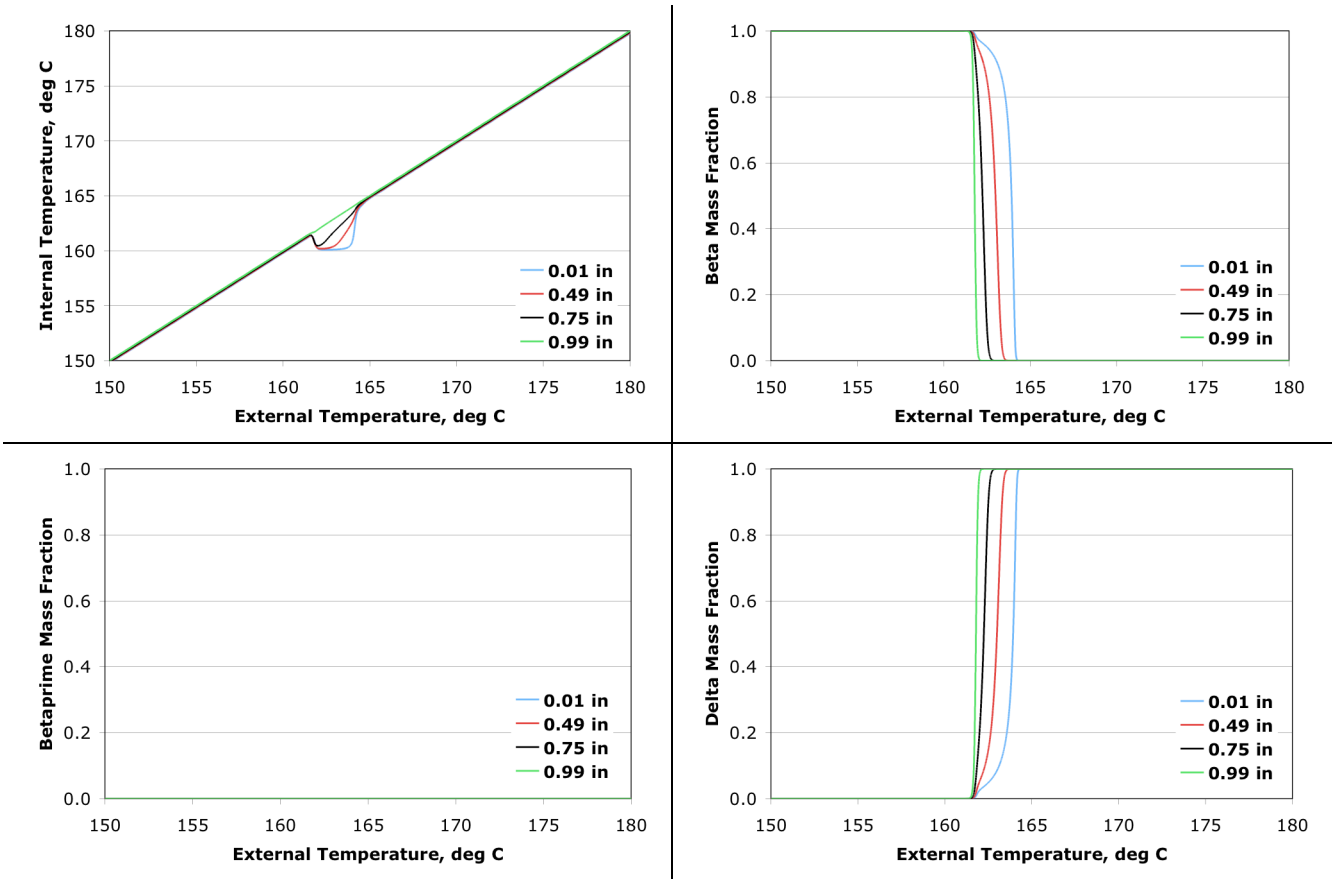

FIGURE 32. External temperature and phase mass fraction history curves as a function of radial position using bidirectional kinetics Model 2 for the STEX experimental scenario. Kinetic parameters were calibrated using the SITI scenario.

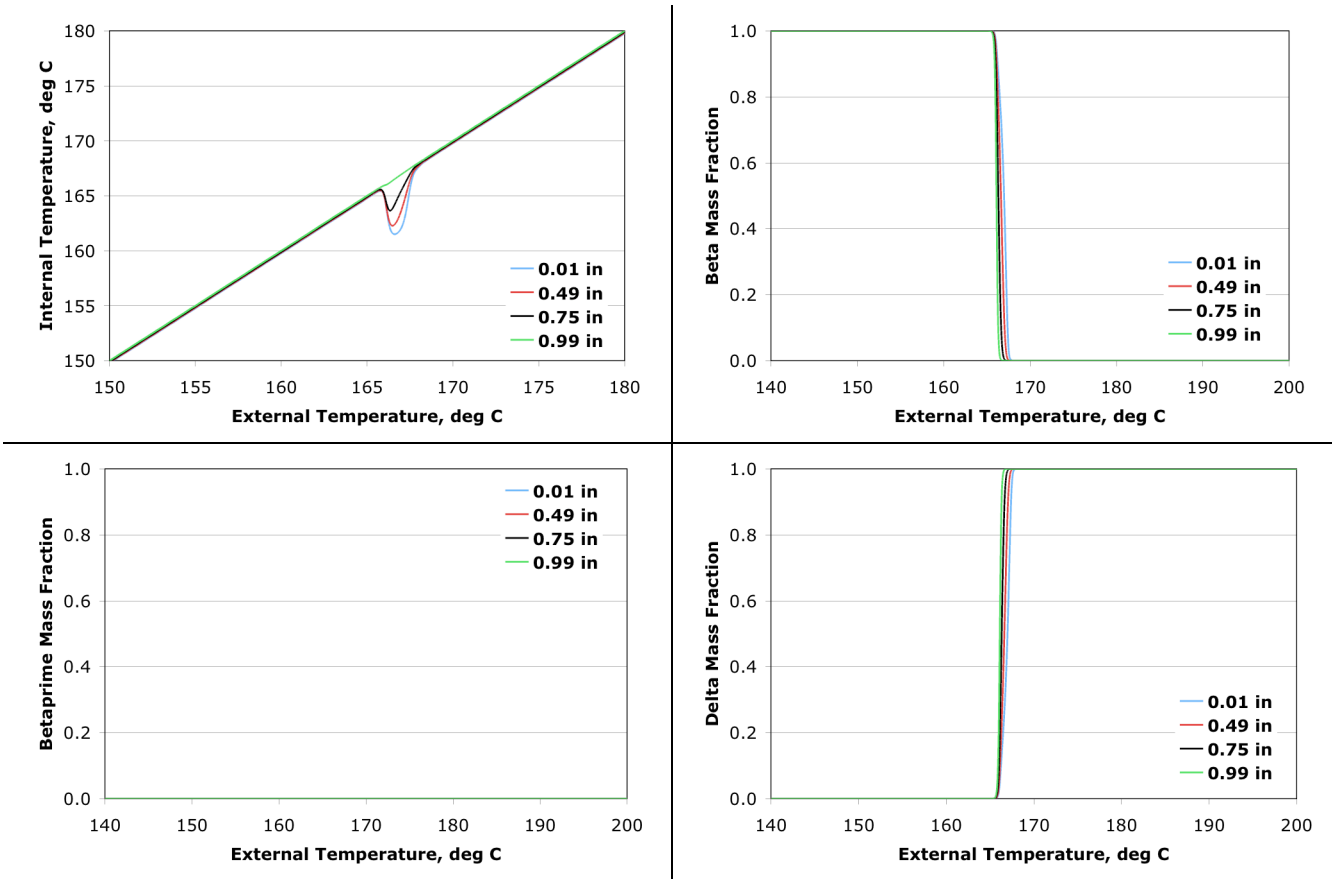

FIGURE 33. External temperature and phase mass fraction history curves as a function of radial position using bidirectional kinetics Model 3 for the STEX experimental scenario. Kinetic parameters were calibrated using the 165°C XRD scenario.

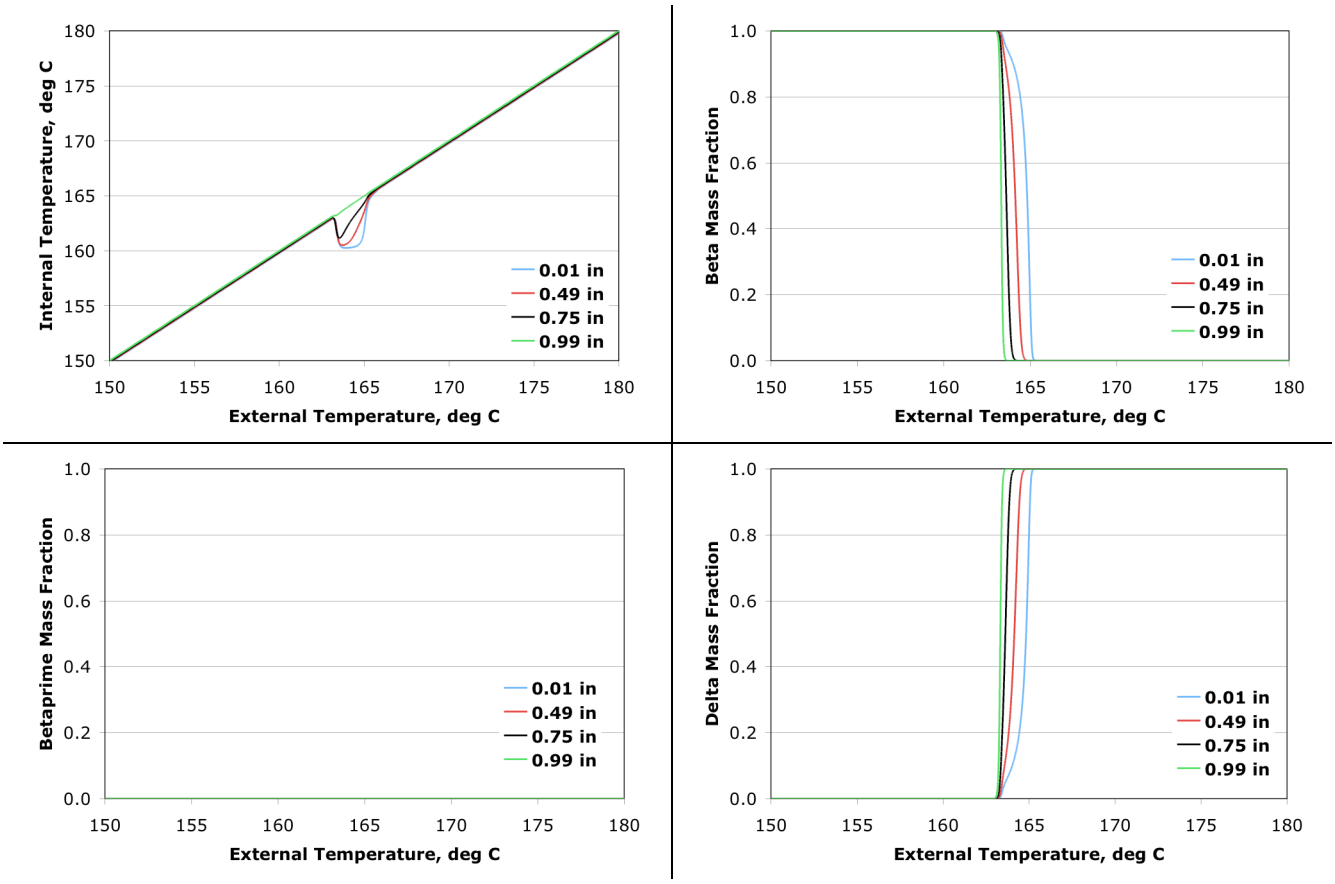

FIGURE 34. External temperature and phase mass fraction history curves as a function of radial position using bidirectional kinetics Model 3 for the STEX experimental scenario. Kinetic parameters were calibrated using the SITI scenario.

Computational Effort Comparison

Simulations of the XRD geometry proved to be very fast, while the SITI and STEX geometries required a relatively large amount of computational effort. The long time for simulations of the SITI geometry is due to the relatively large number of elements in its mesh. The STEX simulations required small thermal tolerances to reduce noise in comparing internal to external temperature values, and tightening the tolerance increased the number of time steps to complete the necessary 200 simulated hours. The XRD geometries used thermal tolerances equivalent to that for the STEX, but the time needed to run was generally less than 5 simulated hours.

If the beta-delta transition kinetics described in this study were to be used in a large-scale simulation, then the computational efficiency of such simulations would depend on the effort required to simulate the kinetics. Therefore, the computational effort for all four kinetics was evaluated via a simple simulation similar to the 165°C XRD setup, except with the isothermal surface fixed at 200°C. The simulated time for this setup was 1 hour. This high, fixed surface temperature forces the ALE2D code to increase the computational effort required for chemistry calculations, so these calculations were needed in nearly every time step. A series of 10 sets of simulations was run for determination of the computational effort required for each kinetics model. Each set included a simulation using each kinetics model, including two for each bidirectional kinetics model (one for the SITI basis, one for the 165°C XRD basis). Organizing the simulations in this manner minimized the effects of outside influence on processor efficiency.

Table 9 shows that the reversible LANL kinetics model required the most computational effort and Model 1 required the least. The times shown in the table are the total amount of processing time in ALE2D's Chemistry Block divided by the number of calls. This is not surprising since the reversible LANL model contained the most reactions (4), while Model 1 contained the least (2). The difference in computational effort between Models 2 and 3 was small, and the difference in calculated values between the 165°C XRD and SITI bases was approximately 10-15%.

In making these comparisons, we emphasize that the issue of computational time is largely decoupled from parameter calibration. Parameters in any of the modeling approaches can be adjusted to fit any particular set of self-consistent experiments. Although they differ in detail, all models are similar enough to mimic the primary features of the phase transition examined to date.

TABLE 9: Computational Effort Required for Chemical Kinetics Modeling

Kinetics Model	Scenario for Calibration of Parameters	Computational effort per call (microseconds)
Reversible LANL	N/A	697
Model 1	165°C XRD	295
	SITI	321
Model 2	165°C XRD	389
	SITI	456
Model 3	165°C XRD	476
	SITI	430

Finally, it should be noted that implementation of the LANL reversible model into ALE2D was more complex than the implementation of the bidirectional models for the SITI and STEX experimental setup scenarios. There were two reasons for this:

- First, the overall time step was reduced to prevent instabilities in the chemistry calculations after the main reaction had taken place. Usage of a larger time step results in the artificial reformation of the beta phase until the point where it instantaneously reacts back to the delta phase.
- Second, the allowable change in composition during a time step was increased for the STEX scenario. The fast kinetics of the model during the STEX simulation caused such a rapid increase in the composition that the code responds by adjusting the kinetics model itself.

Conclusions

This study has provided calibrated parameters for three bidirectional kinetics models for simulating the beta-delta phase transition. The calibration of these parameters depends heavily on the experimental setup scenario by which they are calibrated, where the times associated with the phase transition may differ by an order of magnitude. Generally, those models with parameters calibrated using the SITI data for PBX-9501 are more similar to the LANL reversible model (also calibrated on PBX-9501) than those models with parameters modeled using Zaug's 165°C XRD data. However, calculations using the Reversible LANL model do not agree well with the 165°C XRD experimental findings, indicating that the Reversible LANL model is not accurate for pure HMX formulations. The good agreement between results by the 165°C XRD-based bidirectional models and LX-04 STEX data suggests that these models may be reasonable for modeling experiments using LX-04 material, although the 175°C XRD simulated transitions are longer than observed experiments.

Similarly, the SITI-based bidirectional models provide good approximations for modeling experiments using PBX-9501. However, the authors caution that the primary difference between LX-04 and PBX-9501 is the presence of a nitroplasticizer, which is only one of several variables that has shown to affect transition time, such as particle size (as possibly evidenced by the difference in STEX transition temperatures for LX-04 and LX-10), pressure, and the presence of RDX (Cady and Smith, 1962). In all of the scenarios modeled in this study, the systems were initialized at ambient conditions, pressure dependencies were ignored, and no RDX was present. As more experimental evidence of the beta-delta transition becomes available, the calibrated parameters of these models may be further refined to attain sets of parameters for each important HMX formulation that work for to all geometries.

Acknowledgements

The authors would like to thank Jack Yoh (LLNL) for his work in setting up the HMX materials model in ALE2D, and Al Nichols (LLNL-CCHED) for his work in refining the ALE2D implementation of the LANL reversible kinetics model.

References

Burnham A. K., Weese R. K., Weeks B. L. (2004) A distributed activation energy model of thermodynamically inhibited nucleation and growth reactions and its application to the β→δ phase transition of HMX, J. Chem. Phys. 108, 19443-19441.

Burnham A. K., Weese R. K. (2004) Thermal Decomposition Kinetics of HMX, Lawrence Livermore National Laboratory, Report UCRL-TR-204262 Rev. 1.

Cady H. H., Smith L. C. (1962) Studies on the Polymorphs of HMX, Los Alamos National Laboratory, Report LAMS-2652.

Henson B. F., Smilowitz L., Asay B. W., Dickson P. M. (2002) The beta-delta phase transition in the energetic nitramine octahydro-1,3,5,7-tetranitro-1,3,5,7-tetrazocine: Thermodynamics, J. Chem. Phys. 117, 3780-3788.

Landers A. G. and Brill T. B. (1980) Pressure-temperature dependence of the β→δ polymorph interconversion in octahydro-1,3,5,7-tetranitro-1,3,5,7-tetrazocine, J. Phys. Chem. 84, 3573-3577.

Kaneshige M. J., Renlund A. M., Schmitt R. G., Erikson W. W. (2002) Cook-off experiments for model validation at Sandia National Laboratory, 12th Intl. Det. Symp., San Diego, ONR 333-05-2, pp. 821-830.

Maienschein J.L., Wardell J.F., Reaugh J.E. (2002) Thermal Explosion violence of HMX-based explosives Effect of composition, confinement and phase transition using the scaled thermal explosion experiment, presented at JANNAF 20th Propulsion Systems Hazards Subcommittee Meeting.

Saw C. K. (2002) Kinetics of HMX and phase transitions: effects of grain size at elevated temperature, 12th Intl. Det. Symp., San Diego, Office of Naval Research ONR 333-05-2, pp. 70-78.

Schmitt R. G., Erikson W. W., Kaneshige M. J., Renlund A. M. (2003) An inverse heat transfer analysis of the Sandia Instrumented Thermal Ignition apparatus, JANNAF Joint Meeting, Colorado Springs, SAND2003-4712C.

Tarver C. M. and Tran T. D. (2004) Thermal decomposition models for HMX-based plastic bonded explosives, Comb. Flame 137, 50-62.

Zaug J. M., Farber D. L., Saw C. K., Weeks B. L. (2003) Kinetics of solid phase reactions at high temperature, Lawrence Livermore National Laboratory, Report UCRL-ID-147389 and supplemental viewgraphs.

Urtiew P.A., Forbes J.W., Tarver C.M., Vandersall K.S., Garcia F., Greenwood D.W., Hsu P.C., Maienschein J.L. (2004) Shock sensitivity of LX-04 containing delta phase HMX at elevated temperatures, Shock Compression of Condensed Matter - 2003, Parts 1 and 2, Proceedings 706: 1053-1056, 2004.